J. Mech. Phys. Solids 215 (2026) 106701

Contents lists available at ScienceDirect

Journal of the Mechanics and Physics of Solids

journal homepage: www.elsevier.com/locate/jmps

A micro-macroscopic constitutive model for spatial confinement hydrogels incorporating directional chain slippage and crosslinking distance evolution

Yunqiang Hu [a], Zhaoguo Gao [a], Fei Jia [a,*], Yanju Liu [a], Jinsong Leng [b,*]

[a] Department of Astronautical Science and Mechanics, Harbin Institute of Technology (HIT), P.O. Box 301, No. 92 West Dazhi Street, Harbin, 150001, PR China

[b] Center for Composite Materials and Structures, Science Park of Harbin Institute of Technology (HIT), P.O. Box 3011, No. 2 YiKuang Street, Harbin, 150080, PR China

ARTICLE INFO

Keywords:
Spatial confinement hydrogels
Directional chain slippage
Crosslinking distance evolution
Hyperelastic-to-viscoelastic transition

ABSTRACT

Spatial confinement hydrogels (SCHs) exhibit excellent mechanical properties, including enhanced toughness, self-healing capacity, and swelling-induced degradation, all of which stem from their unique network structures. In these structures, tangential and normal displacements at crosslinking points govern chain slippage and crosslinking distance evolution, yielding variable Kuhn segment numbers and non-zero crosslinking distances overlooked in classical models. This study proposes a micro-macroscopic constitutive model to capture the response of SCHs under large deformation. We first derive an entropic free energy function for individual chains to account for the evolution of the Kuhn segment number. By incorporating finite crosslinking distances into a micro-macroscopic transition model, we develop a macroscopic continuum model that features non-affine deformation mapping and evolution equations for both the Kuhn segment vector and the crosslinking distance. Our analysis reveals that directional chain slippage and crosslinking distance evolution collectively mitigate stress concentrations in SCHs under large strains. Furthermore, the model characterizes the strain rate-dependent behavior of SCHs, specifically the transition from a hyperelastic-dominated to a viscoelastic-dominated regime. The proposed constitutive model provides a valid description of SCH mechanical behavior and may advance engineering applications for hydrogels.

1. Introduction

Hydrogels are three-dimensional (3D) network materials composed of hydrophilic polymer chains and water (Ho et al., 2022; Hu et al., 2023a; López-Díaz et al., 2024), where macroscopic mechanical properties are fundamentally governed by their network structure. This structure is primarily determined by the inter-chain connectivity established during polymerization process. Specifically, after monomers form polymer chains, various solidification mechanisms, including crosslinking, entanglement, sliding-ring, and spatial confinement (Fig. 1(a)), facilitate the construction of a 3D network (Xu et al., 2023; Sun et al., 2023). These mechanisms are distinguished by the tangential and normal mobility of chains at junction points, which leads to distinct variations in mechanical strength, swelling capacity, degradation and strain rate sensitivity (Deng et al., 2021; Jeon et al., 2017; Lifwergren et al., 2025; Li and Gong, 2024; Wang et al., 2025, 2023a).

* Corresponding authors.
E-mail addresses: feijia@hit.edu.cn (F. Jia), lengjs@hit.edu.cn (J. Leng).

https://doi.org/10.1016/j.jmps.2026.106701
Received 4 December 2025; Received in revised form 22 April 2026; Accepted 31 May 2026
Available online 4 June 2026

Crosslinking is the fundamental mechanism of solidification, endowing hydrogels with mechanical stability by forming stable junctions within the polymeric network. To date, most experimental and theoretical efforts on hydrogels are dedicated to understanding and developing crosslinked networks (Hong et al., 2008, 2009; Zhu and Zhong, 2020; Wang et al., 2017). In such a network-solidification mode, polymer chains are excessively constrained at their junctions. The chain segments can hardly adjust to the deformation state before crosslinking breakage. Entanglement represents another type of interchain connection that coexists with crosslinking (Pensalfini et al., 2023; Panyukov, 2023). This connection mode imposes fewer restrictions on chain motion compared to crosslinking, resulting in enhanced mechanical performance in networks dominated by entanglement-mediated physical interactions (Kim et al., 2021; Li et al., 2022; Liu et al., 2023; Zheng et al., 2022). Nevertheless, prior to failure at the crosslinking junctions, constitutive models for both entanglement and crosslinking modes typically assume a constant number of chain segments and a zero spatial distance between crosslinking points (Flory and Rehner, 1943; Edwards and Vilgis, 1988; Wang et al., 2023b; Hui and Long, 2012; Shi et al., 2023; Zhong et al., 2023; Assadi et al., 2025; Liu et al., 2025).

Unlike conventional crosslinking strategies, the sliding-ring connection in networks confines polymer chains via movable rings, which not only imparts solid properties for polymers but also permits chain sliding along the tangential direction (Okumura and Ito, 2001; Ito, 2007). This design enables the network to adjust its chain segment under deformation, leading to stress homogenization, energy dissipation, high elasticity, and thus superior mechanical performance (Chen et al., 2023; Xing et al., 2022a; Jiang et al., 2018; Li and Gong, 2024; Koga and Tanaka, 2005). Ito (2007) introduced the concept of the alignment entropy of cyclic molecules and explained the pulley effect (Mayumi et al., 2012). By incorporating the topological knot theory, Xing et al. (2022b) introduced circulation numbers and moments to describe slide-ring gel performance, linking the sliding mechanism to macroscopic super toughness and deformability. The above models do not take into account the dissipation mechanism of chain sliding and the macroscopic deformation rate dependent mechanical response of hydrogels. Lu and Chen (2023) demonstrated that molecular friction and its dependence on normal force are the root causes of viscoelastic dissipation under large deformations. A comprehensive theoretical model for sliding-ring networks that takes into account dissipative effects was proposed based on the transient network model (Vernerey and Lamont, 2021). This model develops a consistent tensorial constitutive framework for sliding-ring hydrogels, incorporating a physical description of sliding-induced dissipation to characterize the macroscopic response of networks with dangling ends under moderate deformations.

By utilizing ion-chain interactions to confine molecular chains within localized crosslinking domains (hereafter referred to as crosslinking points), spatial confinement hydrogels (SCHs) combine the characteristic mechanics of sliding-ring gels with self-healing and swelling-induced degradation (Wang et al., 2023a). However, their constitutive modeling is complicated by inconsistencies with classical assumptions of uniform segment numbers and zero cross-linking distances. Recent advances have begun to address these complexities. Vernerey and Lamont (2021) utilized Gaussian statistical mechanics to quantify how spatially homogeneous segment distribution, induced by dangling chains, modulates the macroscopic shear modulus, while Lamont et al. (2023) developed a micro-mechanical framework incorporating finite crosslinking distances to analyze the fracture mechanisms of sliding-ring chains. Despite these insights, existing models typically assume spatially uniform segments. This neglects the coupled effects of segment inhomogeneity and non-zero crosslinking distances on the mechanical response of SCHs in the large deformation regime.

As depicted in Fig. 1(b), spatial confinement networks exhibit a self-adaptive stress response through the synergistic reorganization of chain segments and crosslinking distances. This structural reconfiguration promotes a more homogeneous force distribution across chains, maintaining the network in a lower energy state and conferring superior fracture toughness. Fig. 1(c) illustrates the mechanisms of directional chain slippage and crosslinking distance evolution, alongside their respective impacts on the stress-strain response. While these effects are negligible under moderate deformation, they significantly mitigate stress accumulation at large strain. Notably, the dominant mechanism suppressing stress hardening shifts with increasing deformation: chain slippage prevails initially, whereas the evolution of crosslinking distance becomes predominant as slippage approaches saturation. In this work, a micro-macroscopic constitutive model is developed for SCHs, accounting for variable chain segment number and non-zero crosslinking distance. At the microscopic scale, the entropic contribution and the free energy function for chains with variable segment numbers are derived using Langevin statistics (Kuhn and Grün, 1942; Wall and Flory, 1951). Following classical micro-macroscopic transition frameworks (Wang and Guth, 1952; Arruda and Boyce, 1993; Miehe et al., 2004), a non-affine deformation mapping incorporating non-zero crosslinking distance is formulated. Subsequently, a macroscopic continuum model for SCHs is established, comprising the free energy expression and evolution equations incorporating the chain segment and crosslinking distance. This model elucidates the influence of segment number variation and crosslinking distance evolution on the mechanical response of SCHs, predicting a deformation-induced phenomenological transition from hyperelasticity to viscoelasticity. Model predictions agree well with experimental data, validating the proposed constitutive model. Beyond characterizing these intrinsic deformation mechanisms, this work provides a theoretical foundation for exploring complex phenomena such as unloading-induced instability, self-healing, and swelling-induced degradation.

The remainder of this paper is organized as follows. Section 2 details the development of the constitutive model for SCHs. At the microscopic level, we formulate a single chain free energy function to capture the evolution of chain segments. We then establish a non-affine deformation mapping that accounts for finite crosslinking distances. By integrating these components into a micro-macroscopic transition framework, we derive a continuum model for SCHs, alongside the governing evolution equations for crosslinking distances and chain segments. Section 3 presents model predictions and validates them against experimental data, followed by a discussion on free energy approximations, numerical integration parameters, and alternative micro-macroscopic transformation models. Finally, Section 4 summarizes the key findings and provides an outlook on future research.

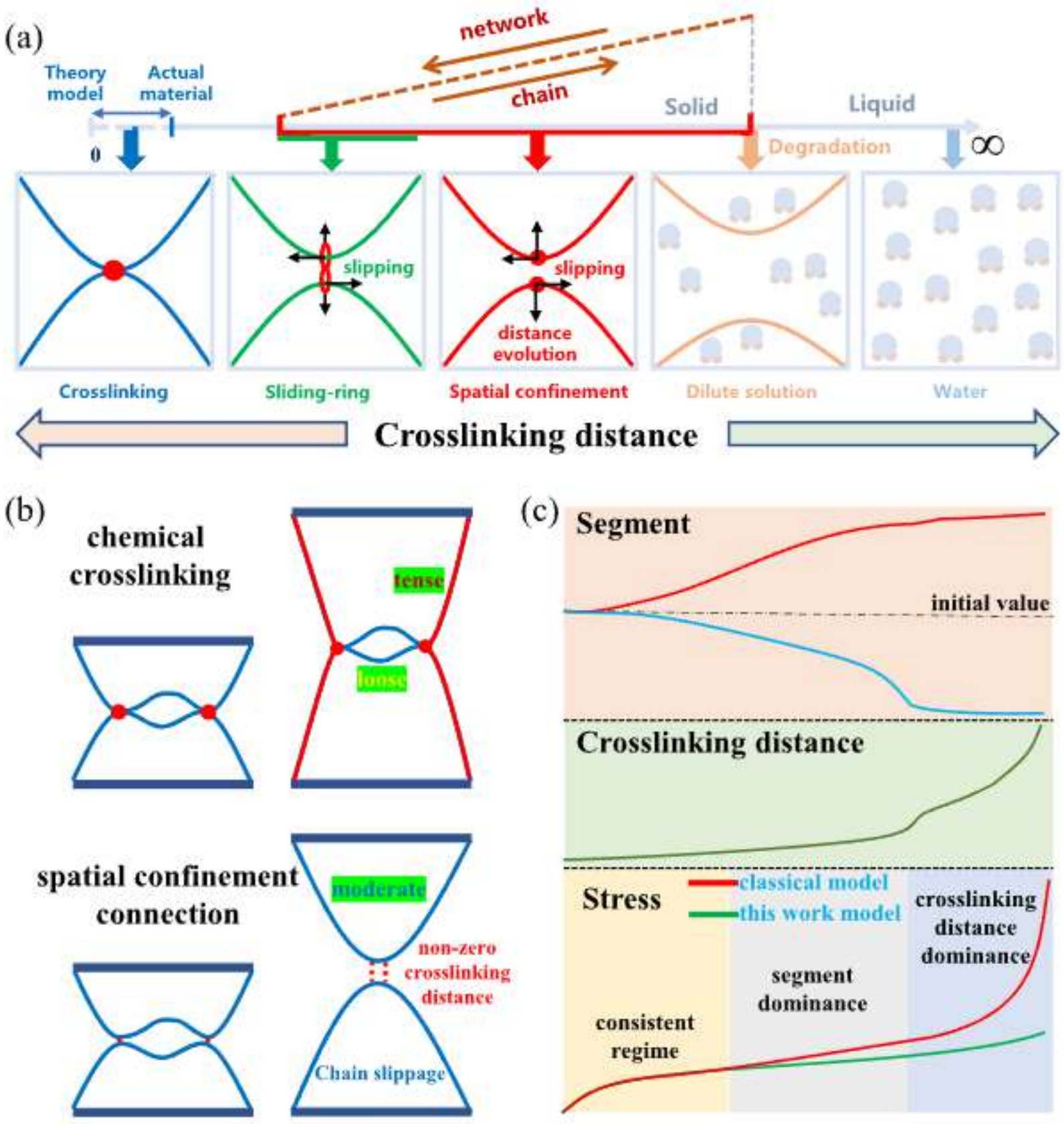

Fig. 1. (a) Network solidification modes and their topologies classified by the crosslinking distance, (b) configurations of chemical crosslinking network and spatial confinement network during the deformation process, and (c) chain segment, crosslinking distance, and stress evolution laws for spatial confinement hydrogels.

2. Constitutive model

2.1. Microscopic model

2.1.1. Statistical description of a chain with variable Kuhn segments

The freely-jointed-chain model is commonly employed to characterize the entropic elasticity of polymer chains (Kuhn and Grün, 1942; James and Guth, 1943). In this model, a chain is assumed to be a connection of N Kuhn segments, and the entropic elasticity stems from the chain conformation, which is modified by the chain's end-to-end distance. Reviewing classical polymer models based on the freely-jointed-chain model, an individual chain is defined as the chain between the two crosslinking points, and the number of Kuhn segments is a constant (Wall and Flory, 1951). For polymer chains subject to spatial confinement crosslinking, the number of Kuhn segments is no longer constant but varies with the deformation state. Herein, we construct the free energy of an individual chain with variable Kuhn segments based on the Langevin statistical function and deduce the evolution equation of the Kuhn segment number.

Let N_0 denote the initial chain Kuhn segment number, and the initial chain length r_0 is $\sqrt{N_0}b$, where b represents the single Kuhn segment length. A stretch ratio $\lambda_c = r/r_0$ is defined to characterize chain deformation, and r is the current chain length. It should

be noted that an individual chain in the SCHs network is not represented by fixed chain segments but by variable chain segments between two spatial confinement crosslinking points. Thus, the stretch ratio of the chain λ_c as described herein can be interpreted as the stretch ratio between two crosslinking points (Vernerey and Lamont, 2021). The relative chain stretch ratio is defined as

$$\Lambda = \frac{r}{Nb} = \sqrt{N_0}\frac{\lambda_c}{N} \tag{1}$$

where the current Kuhn segment number and the Kuhn segment ratio are N and N/N_0, respectively. The chain distribution probability of an individual chain can be described by the following Langevin probability function (Kuhn and Grün, 1942)

$$\begin{aligned} p(r,N) &= p_1(N)p_2(r,N) \\ &= \exp(-\Xi(N))\exp\left[-N\frac{r}{Nb}\beta\left(\frac{r}{Nb}\right) - N\ln\frac{\beta\left(\frac{r}{Nb}\right)}{\sinh\beta\left(\frac{r}{Nb}\right)}\right] \end{aligned} \tag{2}$$

where $\beta(\Re) = L^{-1}(\Re)$, $L(\Re)$ is the Langevin function and $\Xi(N)$ is an intrinsic function of N. In this work, approximation $\beta(\Re) = \Re(3-2.6\Re+0.7\Re^2)/((1-\Re)(1+0.1\Re))$ is utilized (Jedynak, 2015). Unlike the well-defined p_2, p_1 is often treated as a constant function in classical models with a fixed N, and an explicit expression for p_1 has not been formulated (Arruda and Boyce, 1993; Miehe et al., 2004; Xiang et al., 2018). The expression of p_1 is fundamental to describing the behavior of segment evolution, which can be determined by using the normalized constraint condition of the probability function

$$\iint_\Omega \int_0^{r_{max}} p(r,N)r^2 dr d\Omega = 1 \tag{3}$$

where Ω represents the spherical surface and the maximum value of chain length r_{max} corresponds to the chain contour length Nb. Substituting Eq. (2) into Eq. (3), the integration function is then written as

$$\int_0^{Nb} \exp(-\Xi(N)) \times \exp\left(-N\frac{r}{Nb}\beta\left(\frac{r}{Nb}\right) - N\ln\frac{\beta\left(\frac{r}{Nb}\right)}{\sinh\beta\left(\frac{r}{Nb}\right)}\right) r^2 dr = \frac{1}{4\pi} \tag{4}$$

We can obtain $\Xi(N)$ as

$$\Xi(N) = \ln\left[4\pi\int_0^{Nb}\exp\left(-N\frac{r}{Nb}\beta\left(\frac{r}{Nb}\right) - N\ln\frac{\beta\left(\frac{r}{Nb}\right)}{\sinh\beta\left(\frac{r}{Nb}\right)}\right) r^2 dr\right] \tag{5}$$

Combining Eqs. (2) and (5) and with the definition $\psi = -k_B T \ln p(r,N)$, where k_B denotes the Boltzmann constant and T is the absolute temperature, the total chain free energy of an individual chain can be expressed as

$$\begin{aligned} \psi(r,N) &= k_B T \ln\left[4\pi\int_0^{Nb}\exp\left(-N\frac{r}{Nb}\beta\left(\frac{r}{Nb}\right) - N\ln\frac{\beta\left(\frac{r}{Nb}\right)}{\sinh\beta\left(\frac{r}{Nb}\right)}\right) r^2 dr\right] \\ &+ Nk_B T\left[\frac{r}{Nb}\beta\left(\frac{r}{Nb}\right) + \ln\frac{\beta\left(\frac{r}{Nb}\right)}{\sinh\beta\left(\frac{r}{Nb}\right)}\right] \end{aligned} \tag{6}$$

Compared with the classical model, we formulate the free energy contribution arising from changes in the number of segments, which can be used to capture the Kuhn segment evolution of the chain. Combining theoretical analysis with numerical fitting yields an approximation for Eq. (6)

$$\psi(r,N) = k_B T[A(b) + B\ln(N+C)] + Nk_B T\left[\sqrt{N_0}\frac{\lambda_c}{N}\beta\left(\sqrt{N_0}\frac{\lambda_c}{N}\right) + \ln\frac{\beta\left(\sqrt{N_0}\frac{\lambda_c}{N}\right)}{\sinh\beta\left(\sqrt{N_0}\frac{\lambda_c}{N}\right)}\right] \tag{7}$$

The approximation procedure is given in Appendix A, and we found that A is a function of b, but both B and C are constants, wherein $B = 1.5098$ and $C = -0.3943$, which means that the derivative of $\Xi(N)$ with respect to N is only dependent on a simple explicit form of two constants

$$\frac{\partial\Xi(N)}{\partial N} = \frac{B}{N+C} \tag{8}$$

This result allows us to clarify the chain slippage law without needing to determine the value of A. The additional conformation entropy of an individual chain due to variation in chain segments is obtained (Eq. (7)), in which the total entropy is composed of contributions from the stretch ratio λ_c and the segment number N. We can obtain the chain force $f_{chain}b/k_B T$ and the chain slippage driving force $f_\theta/k_B T$ through derivatives of ψ with respect to r and N, respectively

$$\frac{f_{chain}b}{k_B T} = \frac{b}{k_B T}\frac{\partial\psi}{\partial r} = \beta\left(\sqrt{N_0}\frac{\lambda_c}{N}\right) \tag{9}$$

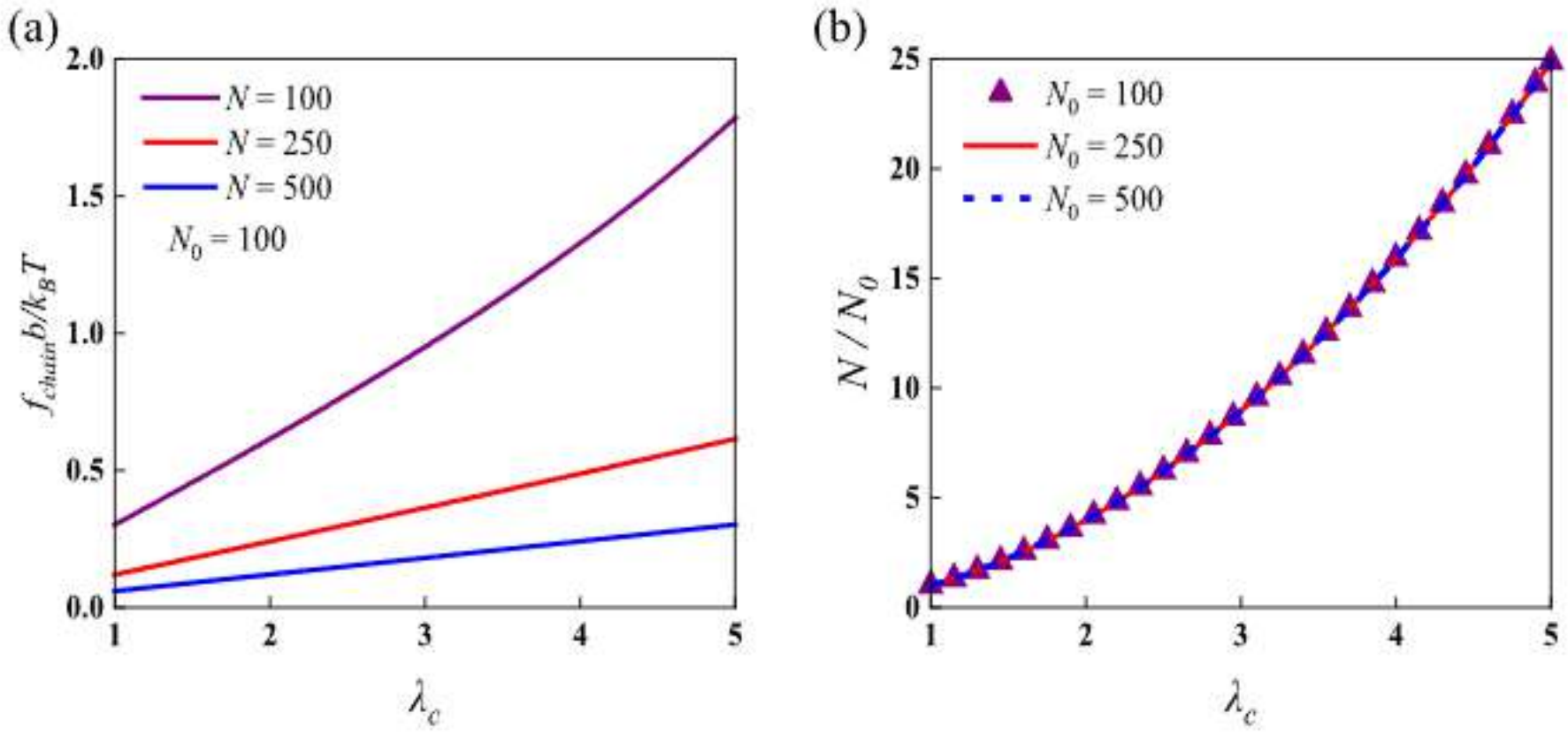

Fig. 2. Results of the chain free energy of an individual chain: (a) the relationship between the chain force $f_{chain}b/k_BT$ and λ_c and (b) $N/N_0 - \lambda_c$ as $f_\theta = 0$.

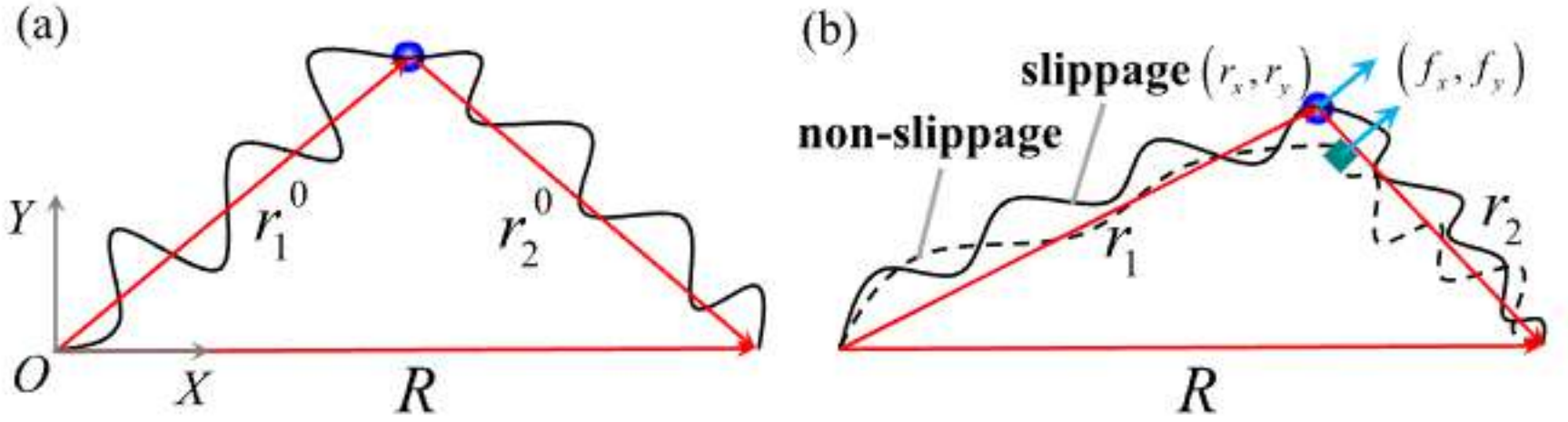

Fig. 3. Schematic diagram of the two-chain system: (a) the initial configuration and (b) the current configuration.

$$\frac{f_\theta}{k_BT} = -\frac{1}{k_BT}\frac{\partial \psi}{\partial N} = -\frac{B}{N+C} - \ln\frac{\beta\left(\sqrt{N_0}\frac{\lambda_c}{N}\right)}{\sinh\beta\left(\sqrt{N_0}\frac{\lambda_c}{N}\right)} \tag{10}$$

As shown in Eq. (9), besides λ_c, the Kuhn segment number N also plays an important role in determining the chain force, and its slippage behavior is governed by Eq. (10). Fig. 2(a) shows that for a given λ_c, consistent with expectations, the chain force decreases with increasing chain length N. Fig. 2(b) depicts the relationship between λ_c and N/N_0 when $f_\theta = 0$, in which N increases with λ_c and the N/N_0 values of all curves are identical. Eq. (7) is the free energy of an individual chain, and in hydrogel networks, the slipping driving force obtained by the crosslinking energy should be involved, and this will be discussed in Section 2.2.

2.1.2. *Chain slippage of a two-chain system*

The free energy and slippage behavior of an individual chain are investigated in Section 2.1.1. It can be observed that the chain deformation can trigger segment slippage, thereby altering the chain force. We now investigate the deformation and slippage of chains within segment conservation systems. Two idealized models are developed, beginning with the simplest case: a two-chain system. As shown in Fig. 3, the two-chain system is composed of two chains with identical initial chain length $r_0^1 = r_0^2$. The right and left ends are fixed, and the two chains contain an equal number of Kuhn segments N_0. When an external force f_E (with horizontal and vertical components f_x and f_y, respectively) is applied to the midpoint of the two-chain system, the location of force moves along the chain and segment evolution occurs.

Upon deformation, the location coordinate of f_E is denoted as (r_x, r_y). Two chain lengths are $r_1 = \sqrt{r_x^2 + r_y^2}$ and $r_2 = \sqrt{(R - r_x)^2 + r_y^2}$, respectively. Based on Eq. (7) and considering the conservation of chain segment, the Lagrangian of the two-chain

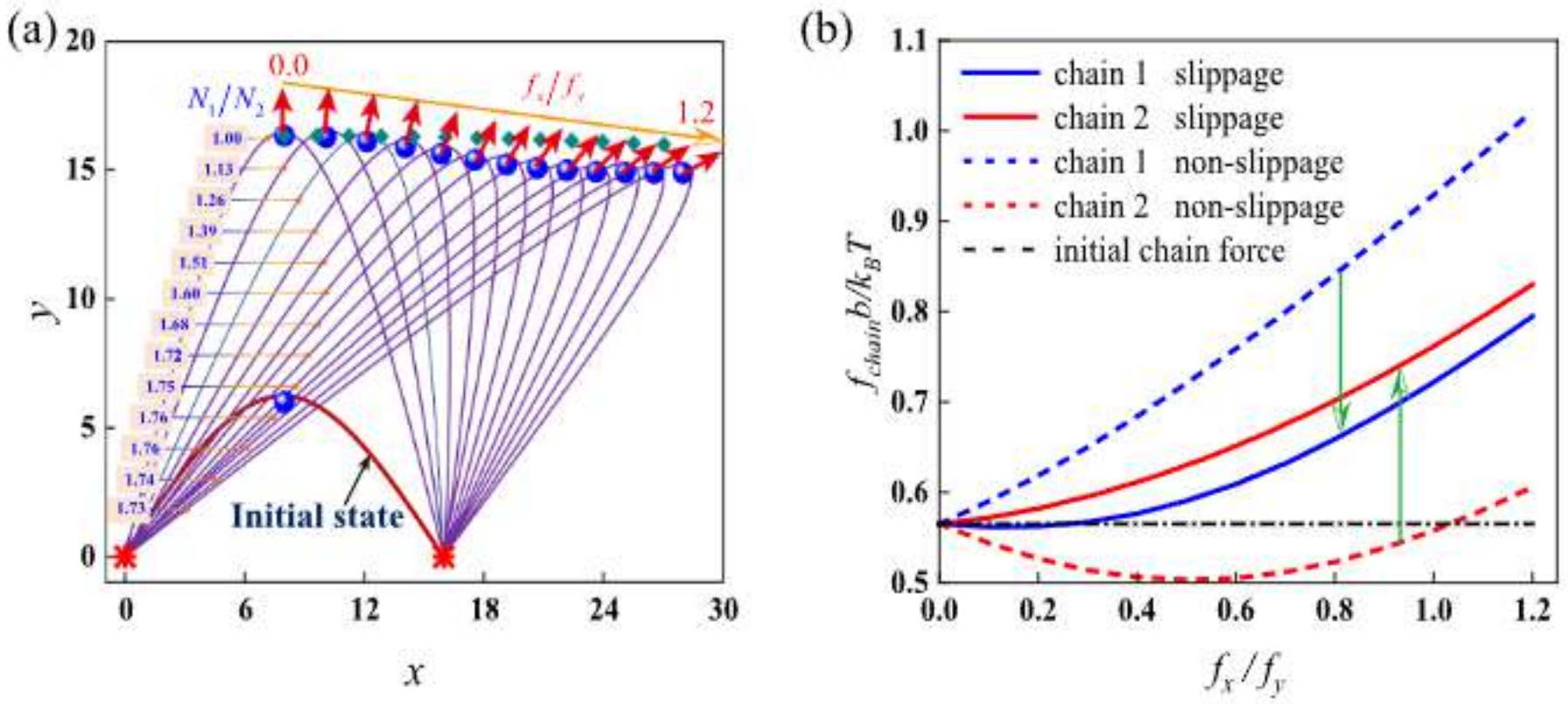

Fig. 4. Numerical results of the two-chain system: (a) locations of crosslinking points in initial and current configurations, where the positions of the two ends and crosslinking points of the two-chain system are connected by spline curves, roughly representing the chain conformations. The segment ratios of the two chains N_1/N_2 are listed. The dark blue rectangles represent the crosslinking point positions of the non-slippage chains after deformation; and (b) curves between $f_{chain}b/k_BT$ and f_x/f_y for slippage and non-slippage conditions, respectively.

system is given as

$$\frac{L}{k_BT} = \Xi(N_1) + N_1\left(\Lambda_1\beta_1 + \ln\frac{\beta_1}{\sinh\beta_1}\right) + \Xi(N_2) + N_2\left(\Lambda_2\beta_2 + \ln\frac{\beta_2}{\sinh\beta_2}\right) + \Pi(N_1 + N_2 - 2N_0) \tag{11}$$

where the Lagrange multiplier Π is introduced to impose chain segment conservation, and the key variables are

$$\begin{aligned} \Lambda_1 &= \frac{\sqrt{r_x^2 + r_y^2}}{N_1}, \qquad \beta_1 = L^{-1}(\Lambda_1) \\ \Lambda_2 &= \frac{\sqrt{(R - r_x)^2 + r_y^2}}{N_2}, \qquad \beta_2 = L^{-1}(\Lambda_2) \end{aligned} \tag{12}$$

Following Eq. (11), the chain slippage governing equations and force equilibrium equations can be deduced as

$$\begin{aligned} \frac{\partial L}{\partial N_1} = 0: &\quad \frac{B}{N_1 + C} + \ln\frac{\beta_1}{\sinh\beta_1} + \Pi = 0 \\ \frac{\partial L}{\partial N_2} = 0: &\quad \frac{B}{N_2 + C} + \ln\frac{\beta_2}{\sinh\beta_2} + \Pi = 0 \\ \frac{\partial L}{\partial \Pi} = 0: &\quad N_1 + N_2 - 2N_0 = 0 \\ \sum f_x = 0: &\quad -\beta_1\frac{r_x}{\sqrt{r_x^2 + r_y^2}} + \beta_2\frac{r - r_x}{\sqrt{(R - r_x)^2 + r_y^2}} + f_x = 0 \\ \sum f_y = 0: &\quad -\beta_1\frac{r_y}{\sqrt{r_x^2 + r_y^2}} - \beta_2\frac{r_y}{\sqrt{(R - r_x)^2 + r_y^2}} + f_y = 0 \end{aligned} \tag{13}$$

The system of equations consists of three components: Eqs. $(13)_1$ and $(13)_2$ govern chain slippage, Eq. $(13)_3$ enforces segment conservation, and Eqs. $(13)_4$ and $(13)_5$ establish force equilibrium at the application point of force along the X and Y directions, respectively. All length quantities, such as r_1, r_2, and R, have been normalized by b. Parameters $R = 16$, $N_0 = 100$ and $f_y = 1$ are utilized. The solution set N_1, N_2, Π, r_x, r_y can be obtained by numerically solving the above equations.

The initial and current configurations of the two-chain system with various f_x/f_y ratios are depicted in Fig. 4(a). The results indicate that the symmetric loading condition ($f_x/f_y = 0$) do not induce chain slippage. A break in symmetry by the external force ($f_x/f_y \neq 0$) induces chain slippage, leading to an increase in N_1/N_2 with increasing force ratio. A fundamental distinction in force distribution exists between non-slippage and slippage two-chain systems, as illustrated in Fig. 4(b). In the non-slippage configuration, taking the state at $f_x/f_f = 0$ as the reference, where both chain 1 and chain 2 are stretched, we find that as f_x/f_f increases, chain 1 bears the majority of the external force under the condition of three-force equilibrium, while chain 2 becomes relatively compressed. As f_x/f_f continues to increase, the distance between the equilibrium position and the end point of the chain further

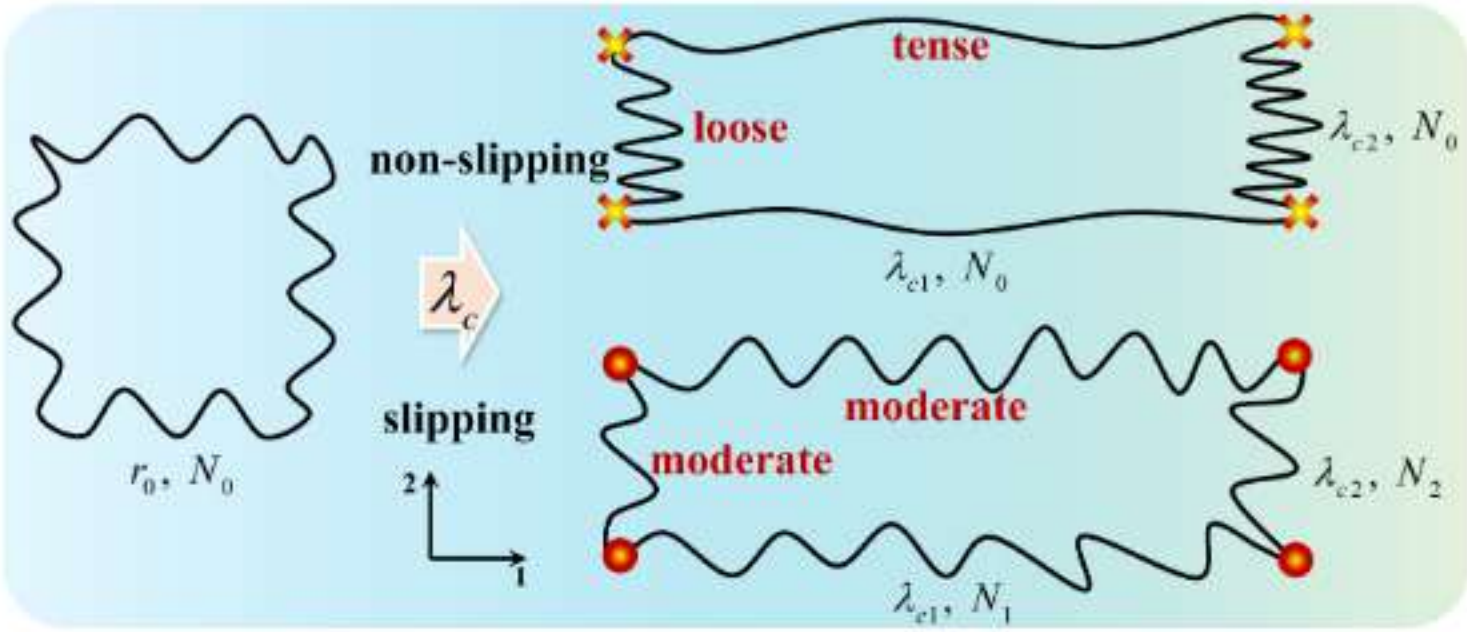

Fig. 5. Deformation schematics of the rectangular loop chain under slippage and non-slippage conditions.

increases, and chain 2 becomes relatively stretched as well. Nevertheless, chain 1 still primarily undertakes the tensile load. In contrast, slippage enables force-amplitude reconfiguration via the adjustment of Kuhn segment lengths between adjacent chains. This adjustment promotes a more homogeneous chain force distribution.

2.1.3. Chain slippage of a rectangular loop chain

To further elucidate the mechanism of chain slippage, the second theoretical example is introduced (Fig. 5). It comprises a closed-loop topology of four chains, each with an initial length r_0 and N_0 Kuhn segments, arranged in an initial square configuration. Deformation is induced by a prescribed displacement along the 1-direction, with the left-hand junctions fixed. Transverse motion remains unrestricted, subject to a pinned junction to preclude rigid-body translation. This setup allows junction-mediated slippage to drive network reconfiguration, which redistributes internal stresses and homogenizes the chain forces.

The rectangular loop chain model is formulated based on single chain free energy and Kuhn segment conservation. For symmetric deformation, the Lagrangian L is given by

$$\frac{L}{2k_BT} = \Xi(N_1) + N_1 kT\left(\Lambda_1\beta_1 + \ln\frac{\beta_1}{\sinh\beta_1}\right) + \Xi(N_2) + N_2\left(\Lambda_2\beta_2 + \ln\frac{\beta_2}{\sinh\beta_2}\right) + \Pi\left(N_1 + N_2 - 2N_0\right) \tag{14}$$

where $\Lambda_1 = \sqrt{N_0}\lambda_{c1}/N_1$, $\beta_1 = L^{-1}(\Lambda_1)$ and $\Lambda_2 = \sqrt{N_0}\lambda_{c2}/N_2$, $\beta_2 = L^{-1}(\Lambda_2)$. The chain stretch are $\lambda_{c1} = \lambda_c$ and $\lambda_{c2} = \lambda_c^{\nu}$, respectively. The purpose of introducing the parameter ν is to describe the ratio of the stretch ratios in directions 1 and 2 ($\nu = -0.5, 0.0, 1.0$), as depicted in Fig. 6(a). Following deformation, the relationship between the normalized system energy, defined as $E =: \psi/2k_BT - 2A(b)$, and the segment ratio N_1/N_2 is depicted in Fig. 6(b). Results indicate that, except for $\nu = 1.0$, no deformation mode minimizes the free energy in the absence of slippage. The mechanism of segment slippage is determined by the minimization of free energy. While fixed crosslinks in conventional networks impose topological constraints that preclude the global energy minimum, sliding crosslinks allow the system to reach minimum energy state through segment redistribution.

The governing equations for the rectangular chain system are derived by taking the partial derivatives of the Lagrangian L with respect to N_1, N_2 and Π. This procedure yields a set of equations identical to the first three expressions in Eq. (13). Solving this system provides the values for the segment numbers, N_1 and N_2. As shown in Fig. 6(c), deformation induces a non-uniform distribution of Kuhn segments through an increase in N_1 and a decrease in N_2, implying directional slippage toward chains under higher stretch. Fig. 6(d) compares the chain forces in networks with and without chain slippage. We find that directional chain slippage delays the onset of strain hardening, thereby mitigating the abrupt rise in chain force that typically precipitates rupture. This mechanism has profound implications for macroscopic elastomers, which are characterized by an inherent non-uniformity in chain length. Slippage enables shorter, more strained chains to effectively borrow segments from less strained ones, thus alleviating their load. Chain slippage overcomes the classical limitation where a chain stretch ratio cannot exceed the square root of its initial segment number. By allowing segments to redistribute, this mechanism enables individual chains to achieve higher effective stretches.

2.2. Continuum model based on the micro-macroscopic transition

Section 2.1 formulates the entropic free energy accounting for Kuhn segment variations. To bridge the scales for SCHs, a continuum-level model is constructed through the micro-macroscopic transition strategy. This involves establishing a correspondence between microscopic quantities such as the chain stretch λ_c and segment number N and macroscopic quantities including the deformation gradient $\mathbf{F}$ and the Kuhn segment vector $\mathbf{N}$. In addition, the crosslinking distance d is incorporated to capture network characteristics not inherent in single-chain models. The constitutive model for SCHs is thus formulated in terms of $\mathbf{F}$, $\mathbf{N}$ and d. A non-equilibrium constitutive model framework is established in Section 2.2.1, which gives fundamental constraints of the constitutive model. The free energy expression is given in Section 2.2.2, where the microsphere micro-macroscopic transition model is used. Based on the features

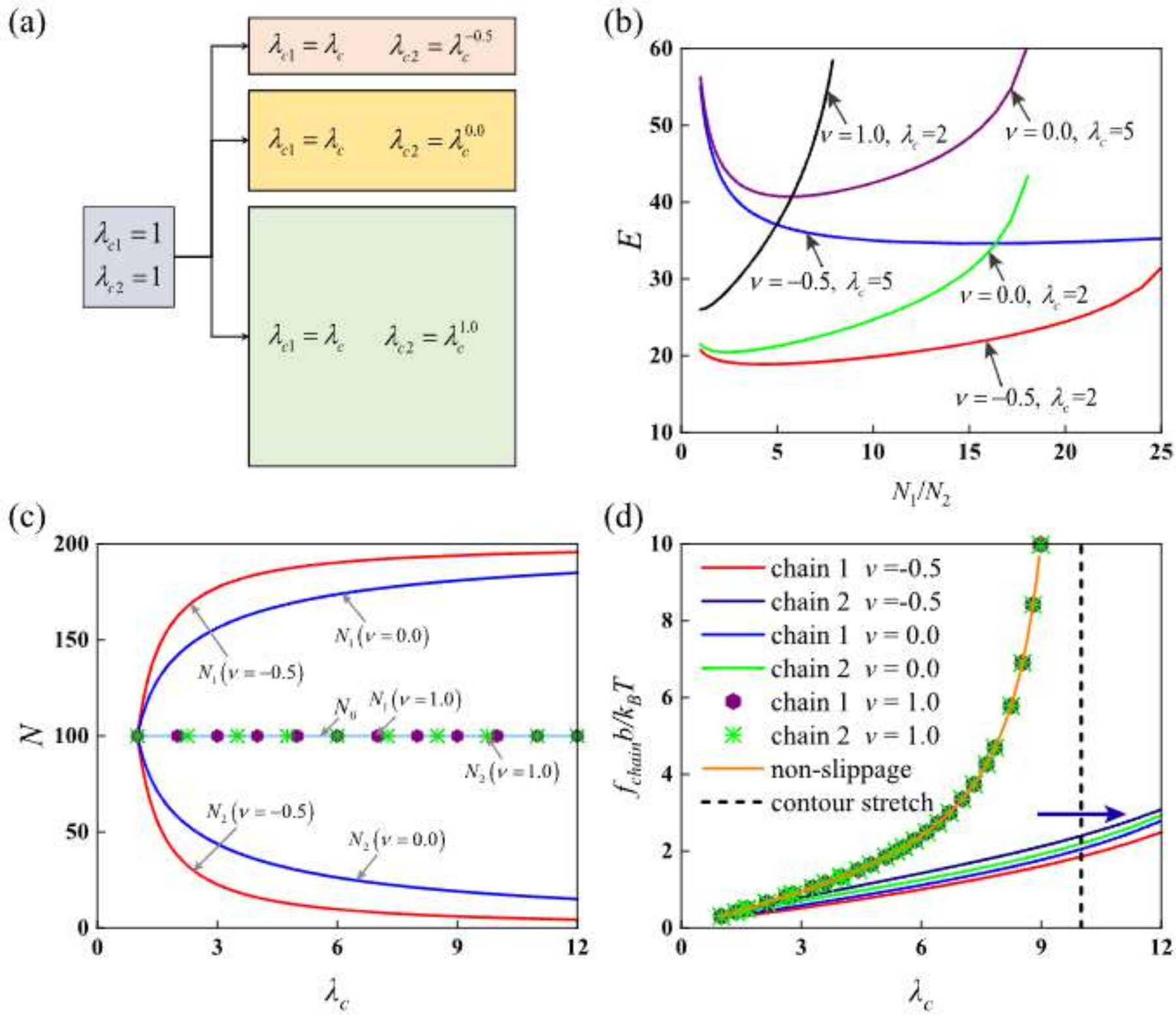

Fig. 6. Results of the rectangular loop chain: (a) deformation diagrams with various ratios of the stretch ratios in directions 1 and 2, (b) system energy $E =: \psi/2k_BT - 2A(b)$ as a function of Kuhn segment ratio N_1/N_2, where the redistribution of chain segments can drive the system towards a state of lower energy, (c) segment evolution during deformation process, and (d) chain force $f_{chain}b/k_BT$ as a function of λ_c.

of the spatial confinement network, a non-affine deformation transformation model considering the crosslinking distance is proposed in Section 2.2.3. Section 2.2.4 derives the stress and evolution equations for **N** and d. Section 2.2.5 provides a numerical algorithm for the constitutive model.

2.2.1. *Thermodynamic framework*

The mechanical response of conventional elastomers is generally treated as time independent, with chains undergoing instantaneous conformational adjustments to the stress state. In contrast, SCHs exhibit time dependence arising from polymer chain slippage. This rate sensitive response is demonstrated by uniaxial tensile and stress relaxation experiments at different strain rates, as detailed in Section 3.2. In the present section, a non-equilibrium macroscopic model is established to capture the rate dependent chain slippage and stress response. This work aims to elucidate the behaviors of network deformation and chain slippage in SCHs under constant water content, assuming constant mixture and ion free energies. This assumption is justified by two factors. First, the spatial confinement network more effectively restricts water and ion diffusion than conventional acrylamide hydrogels (Wang et al., 2023a). Second, the short experimental timescale is negligible compared to the diffusion time (Xu et al., 2024). The thermodynamic laws governing the constitutive model are expressed as Zhang et al. (2025), Hu et al. (2023b)

$$\dot{W} - \frac{1}{2}\mathbf{T} : \dot{\mathbf{C}} \leq 0 \tag{15}$$

where W represents the free energy density, $\mathbf{T}$ is the second P-K stress and $\mathbf{C} = \mathbf{F}^T\mathbf{F}$ denotes the right Cauchy-Green tensor. Considering W is a function of $\mathbf{C}$, $\mathbf{N}$, and d, Eq. (15) can be modified as

$$\left(\frac{\partial W(\mathbf{C},\mathbf{N},d)}{\partial \mathbf{C}} - \frac{1}{2}\mathbf{T}\right) : \dot{\mathbf{C}} + \frac{\partial W(\mathbf{C},\mathbf{N},d)}{\partial \mathbf{N}} \bullet \dot{\mathbf{N}} + \frac{\partial W(\mathbf{C},\mathbf{N},d)}{\partial d}\dot{d} \leq 0 \tag{16}$$

An analysis of the stationarity of the equation, specifically setting the first and third terms to zero, yields the definition of the Cauchy stress σ and the governing equation for d, respectively

$$\boldsymbol{\sigma} = 2\mathbf{F}\frac{\partial W(\mathbf{C},\mathbf{N},d)}{\partial \mathbf{C}}\mathbf{F}^T \tag{17}$$

$$\frac{\partial W(\mathbf{C},\mathbf{N},d)}{\partial d} = 0 \tag{18}$$

In SCHs, chain slippage drives the evolution of chain segments, the dissipative mechanism analogous to those in slide-ring hydrogels and viscoelastic polymers (Vernerey and Lamont, 2021; Miehe and Göktepe, 2005) and such dissipative processes are commonly modeled using a dissipative potential (Ziegler and Wehrli, 1987). Accordingly, we derived the evolution equation of $\mathbf{N}$ by introducing a dissipative potential ϕ

$$\frac{\partial W(\mathbf{C},\mathbf{N},d)}{\partial \mathbf{N}} + \frac{\partial \phi}{\partial \dot{\mathbf{N}}} = 0 \tag{19}$$

As demonstrated in Section 3.2, this framework effectively captures the mechanical response of polyacrylamide hydrogels. Based on Eqs. (16)–(19), ϕ complies with

$$\frac{\partial \phi}{\partial \dot{\mathbf{N}}} \bullet \dot{\mathbf{N}} \geq 0 \tag{20}$$

To ensure the satisfaction of Eq. (20), we assume

$$\frac{\partial \phi}{\partial \dot{\mathbf{N}}} = k_S\dot{\mathbf{N}} \quad (k_S > 0) \tag{21}$$

where k_S can be seen as the chain slippage friction coefficient (Vernerey and Lamont, 2021). In accordance with Eqs. (19) and (21), the evolution equation of $\mathbf{N}$ is governed by

$$\frac{\partial W(\mathbf{C},\mathbf{N},d)}{\partial \mathbf{N}} + k_S\dot{\mathbf{N}} = 0 \tag{22}$$

2.2.2. Free energy

To account for chain stretch and alterations in crosslinking distance, the free energy of SCHs is decomposed into

$$W(\mathbf{C},\mathbf{N},d) = W_{net}(\mathbf{C},\mathbf{N},d) + W_c(d) \tag{23}$$

where W_{net} denotes the free energy of the network and W_c represents the free energy of the crosslinking point. W_{net} is the sum of the chain free energy and it can be obtained through combining the free energy of a single chain and a micro-macroscopic transition model. In contrast to three chain or eight chain models, the microsphere model is better suited to characterize the mechanics of spatial confinement hydrogels, as it naturally accommodates full tensor representations and captures directional chain slippage in a physically consistent manner (Miehe et al., 2004; Xiao et al., 2021). Accordingly, the microsphere model is adopted for the micro-macroscopic transition, and alternative models are further discussed comparatively in Section 3.4.4. While the deformation and slippage of microscopic chain systems can be characterized, tracking every chain within SCH samples remains a significant challenge. The microsphere model addresses this difficulty by capturing the macroscopic mechanics of SCHs through the evaluation of chain deformation and slippage along a finite set of spatial orientations (Fig. 7). In the initial configuration, the orientation of sub-chains within a chain is uniformly distributed among the sphere's kinematically active directions and chains stretch and slippage are governed by intrinsic limitations defined by the microsphere model. Consequently, the network free energy of SCHs is defined as

$$\begin{aligned} W_{net}(\mathbf{C},\mathbf{N},d) &= \iint_S \sum_{i=1}^{M} \psi(\lambda_{ci}, N_i)dn = \langle nM\psi(\lambda_c, N)\rangle \\ &= \frac{nMk_BT}{|\Omega|}\iint [A + B\ln(N(\mathbf{n}) + C)]d\Omega \\ &\quad + \frac{nMk_BT}{|\Omega|}\iint N(\mathbf{n})\left[\frac{\lambda_c(\mathbf{n},d)}{N(\mathbf{n})}\sqrt{N_0}\beta\left(\frac{\lambda_c(\mathbf{n},d)}{N(\mathbf{n})}\sqrt{N_0}\right) + \ln\frac{\beta\left(\frac{\lambda_c(\mathbf{n},d)}{N(\mathbf{n})}\sqrt{N_0}\right)}{\sinh\beta\left(\frac{\lambda_c(\mathbf{n},d)}{N(\mathbf{n})}\sqrt{N_0}\right)}\right]d\Omega \end{aligned} \tag{24}$$

where $\mathbf{n}$ is the unit direction vector, n represents the chain crosslinked density, M is the sub-chain number in a chain, Ω denotes the unit sphere and its surface area is $|\Omega| = 4\pi$. As established in the preceding analysis, the sub-chains within the network are randomly oriented in the initial configuration, which yields an isotropic chain network. However, inhomogeneous deformation within the SCH lead to directional variations in chain segment numbers, thereby inducing an anisotropic segmental distribution. $\mathbf{N}$ is the segment

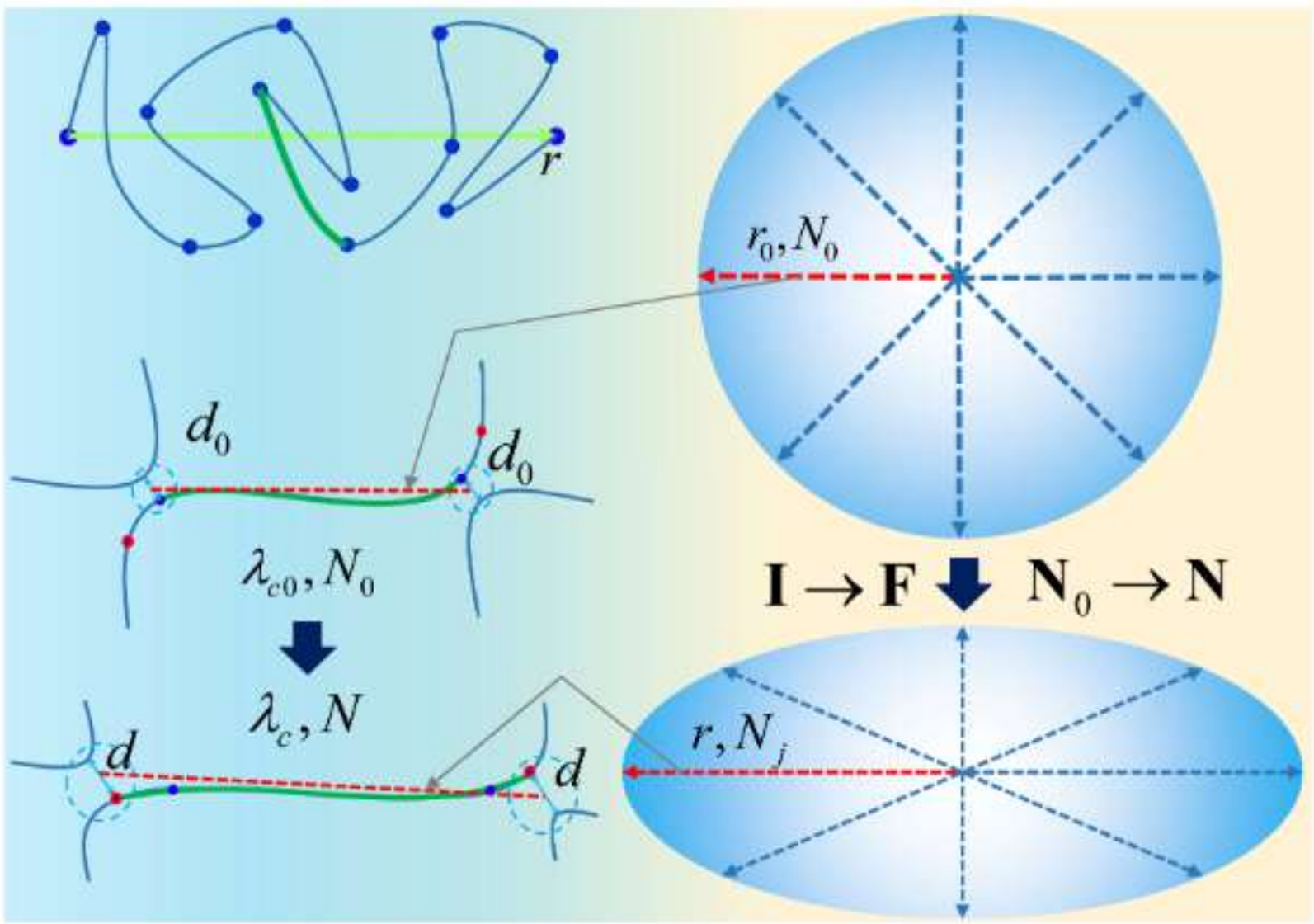

Fig. 7. Schematic diagram of the micro-macroscopic transition, where sub-chains are distributed along the integration directions of the microsphere model. During deformation, both the chain length and orientation can adjust. Additionally, there is a discrepancy between the affine deformation mapping and actual chain stretch due to the non-zero crosslinking distance.

vector composed of the chain segments in each spatial direction and is defined as $[N_1, N_2, \ldots, N_Q]$, where N_j is the Kuhn segment in the j−direction and Q is the total number of integral directions in the microsphere model.

The deformation of the spatial confinement network leads to changes in the crosslinking distance, contributing to the junction free energy W_c. Since the chain slippage mechanisms are material-specific (Ito, 2007; Wang et al., 2023a), we employ a linear spring model that provides a universal framework, thereby focusing on the common physical principles underlying various chain slippage systems. Then W_c is defined as Lamont et al. (2023)

$$W_c = \frac{1}{2}\chi\left(d - d^0\right)^2 \tag{25}$$

where χ represents the stiffness coefficient of the crosslinking point and d^0 is the crosslinking distance in the chain force-free state. Substituting Eqs. (24) and (25) into Eq. (23), the expression for the total free energy of SCHs considering the conservation of segments can be expressed as

$$\begin{aligned} W(\mathbf{C}, \mathbf{N}, d; t) = {} & nMk_BT \sum_{j=1}^{Q} \left[A + B\ln(N_j + C)\right] w_j \\ & + nMk_BT \sum_{j=1}^{Q} N_j \left[\frac{\lambda_{cj}}{N_j}\sqrt{N_0}\beta\left(\frac{\lambda_{cj}}{N_j}\sqrt{N_0}\right) + \ln \frac{\beta\left(\frac{\lambda_{cj}}{N_j}\sqrt{N_0}\right)}{\sinh\beta\left(\frac{\lambda_{cj}}{N_j}\sqrt{N_0}\right)} \right] w_j \\ & + \frac{1}{2}\chi\left(d - d^0\right)^2 + \Pi_N\left(\sum_{j=1}^{Q} N_j - QN_0\right) \end{aligned} \tag{26}$$

The governing principle of directional chain slippage dictates that the orientational distribution of network segments should undergo continuous evolution to accommodate the imposed macroscopic deformation, while adhering to the physical constraint that the total number of segments remains invariant.

2.2.3. *Non-affine micro-macroscopic transition model*

In conventional polymer networks, the two ends of a chain converge at crosslinking points. These points are typically modeled as rigid junctions: the connected chain segments are immobilized in their tangential orientations, preventing relative movement. In the

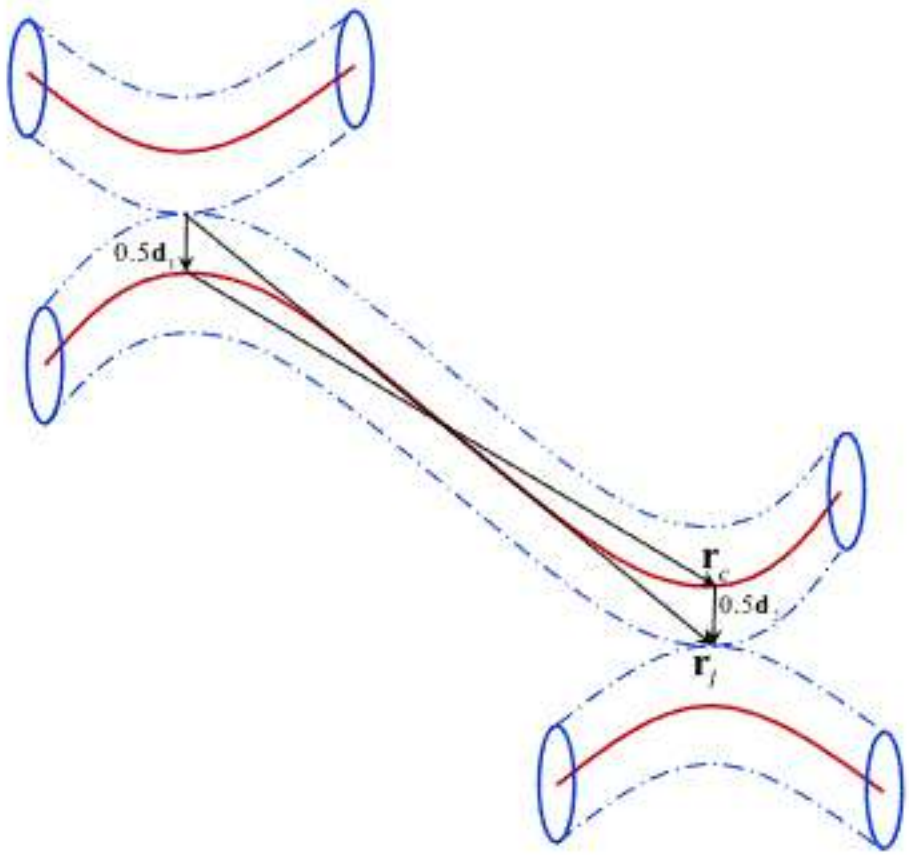

Fig. 8. Geometry of the non-affine micro-macroscopic deformation mapping. $\mathbf{r}_l$ represents the affine length vector determined by macroscopic geometry, $\mathbf{r}_c$ denotes the chain length vector, and $\mathbf{d}_1, \mathbf{d}_2$ are crosslinking distance vectors.

normal direction, the crosslinking distance at the crosslinking point is approximated as zero and assumed constant under deformation. These conditions are inapplicable to SCH networks, and a refined theoretical model of SCHs is required. A model involving chain tangential slippage has been developed in the preceding section. Here, we develop a non-affine micro-macroscopic deformation transition model that incorporates the evolution of the crosslinking distance. In the SCH network, crosslinking distance evolution induces a non-affine micro-macroscopic deformation transition and concurrently alters the chain slippage friction coefficient k_S, thereby modulating chain slippage.

The schematic diagram of the spatial confinement network involving non-zero crosslinking distance is illustrated in Fig. 8, which demonstrates the relationship between the affine deforamtion vector $\mathbf{r}_l$ determined by the macroscopic state and the chain deformation vector $\mathbf{r}_c$

$$\mathbf{r}_l = \mathbf{r}_c + \frac{1}{2}\mathbf{d}_1 + \frac{1}{2}\mathbf{d}_2 \tag{27}$$

where $\mathbf{d}_1$ and $\mathbf{d}_2$ denote the crosslinking distances at the two ends of a chain, respectively. One observes that $\mathbf{r}_l = \mathbf{r}_c$ for $\mathbf{d}_1 = \mathbf{d}_2 = 0$, but $\mathbf{r}_l \neq \mathbf{r}_c$ for non-zero $\mathbf{d}_1$ and $\mathbf{d}_2$. This demonstrates that the non-affine micro-macroscopic deformation transition arises from a non-zero crosslinking distance. The affine stretch ratio between two spatial confinement crosslinking points λ_l is defined as

$$\lambda_l = \frac{|\mathbf{r}_l|}{|\mathbf{r}_{l0}|} = \sqrt{\mathbf{n} \cdot \mathbf{C}\mathbf{n}} \tag{28}$$

where $\mathbf{r}_{l0}$ denotes the chain vector in the reference configuration, corresponding to $\mathbf{r}_l$ in the current configuration. By substituting Eq. (27) into Eq. (28) and introducing the initial chain vector $\mathbf{r}_{c0}$, we have

$$\lambda_l = \frac{|\mathbf{r}_c + \frac{1}{2}\mathbf{d}_1 + \frac{1}{2}\mathbf{d}_2|}{|\mathbf{r}_{c0}|}\left(\frac{|\mathbf{r}_{c0} + \frac{1}{2}\mathbf{d}_{10} + \frac{1}{2}\mathbf{d}_{20}|}{|\mathbf{r}_{c0}|}\right)^{-1} \tag{29}$$

λ_l is further deduced as follows

$$\lambda_l = \sqrt{\frac{\mathbf{r}_c\mathbf{r}_c + (\mathbf{d}_1 + \mathbf{d}_2)\mathbf{r}_c + \frac{1}{4}(\mathbf{d}_1 + \mathbf{d}_2)(\mathbf{d}_1 + \mathbf{d}_2)}{\mathbf{r}_{c0}\mathbf{r}_{c0}}\left(\frac{\mathbf{r}_{c0}\mathbf{r}_{c0} + (\mathbf{d}_{10} + \mathbf{d}_{20})\mathbf{r}_{c0} + \frac{1}{4}(\mathbf{d}_{10} + \mathbf{d}_{20})(\mathbf{d}_{10} + \mathbf{d}_{20})}{\mathbf{r}_{c0}\mathbf{r}_{c0}}\right)^{-1}} \tag{30}$$

Owing to the fact that the crosslinking distance is much smaller than the chain length, the quadratic term in $\mathbf{d}_1 + \mathbf{d}_2$ can be neglected, leading to a simplified relation

$$\lambda_l = \sqrt{\frac{\lambda_c^2 + \lambda_c \alpha \cos\theta}{1 + \alpha_0 \cos\theta_0}} \tag{31}$$

where the length ratio α is defined as $\alpha = d/r_{c0}$ with $d = |\mathbf{d}|$ and $\mathbf{d} = \mathbf{d}_1 + \mathbf{d}_2$. θ is the angle defined by vectors $\mathbf{d}$ and $\mathbf{r}_c$, namely $\cos\theta = (\mathbf{d} \cdot \mathbf{r}_c)/(|\mathbf{d}||\mathbf{r}_c|)$. In the reference configuration, we have $\mathbf{d}_0 = \mathbf{d}_{10} + \mathbf{d}_{20}$, $d_0 = |\mathbf{d}_0|$, $\alpha_0 = d_0/r_{c0}$, and θ_0 is the angle defined

by vectors $\mathbf{d}_0$ and $\mathbf{r}_{c0}$. Combining Eq. (28) and the square root of Eq. (31), λ_c can be deduced as

$$\lambda_c = \frac{-d\cos\theta\alpha_0/d_0 + \sqrt{(d\cos\theta\alpha_0/d_0)^2 + 4(\mathbf{n}\cdot\mathbf{Cn})(1+\cos\theta_0\alpha_0)}}{2} \tag{32}$$

This model involves material parameters α_0 and d_0, and an internal variable d governed by Eq. (18). Additionally, the value of $\cos\theta$ remains to be determined. According to Eq. (27), we obtain the relationship between θ and φ

$$\left(1+\frac{\alpha}{\lambda_c}\cos\theta\right)\cos^2\varphi = \left(\cos\theta+\frac{\alpha}{2\lambda_c}\right)^2 \tag{33}$$

where φ the angle defined by vectors $\mathbf{d}$ and $\mathbf{r}_l$. $\cos\theta$ can then be solved as

$$\cos\theta = -\frac{\alpha\sin^2\varphi}{2\lambda_c} + \frac{\cos\varphi\sqrt{-3\alpha^2+8\lambda_c^2+\alpha^2\cos 2\varphi}}{2\sqrt{2}\lambda_c} \tag{34}$$

Substituting Eq. (34) into Eq. (32) yields

$$\lambda_{cj} = \sqrt{\frac{2\mathbf{n}_j\cdot\mathbf{Cn}_j\left(1+\alpha_0\cos\theta_0\right)+\alpha_0^2\bar{d}^2-2\alpha_0\bar{d}\cos\varphi\sqrt{\mathbf{n}_j\cdot\mathbf{Cn}_j}\sqrt{1+\alpha_0\cos\theta_0}}{2}}, \quad (j=1,2,\ldots,Q) \tag{35}$$

where λ_{cj} denotes the chain stretch ratio in j−direction and $\bar{d} = d/d_0$. The above equation represents the non-affine micro-macroscopic deformation mapping that takes into account the crosslinking distance. This model includes two parameters, α_0 and θ_0, associated with the initial configuration, and two physical quantities, $\bar{d}$ and φ, associated with the current configuration. We first identified the primary factors governing φ, including the deformation gradient $\mathbf{F}$, the orientation vector $\mathbf{n}$ and its initial value φ_0. Dimensional analysis suggests the form $\varphi = \varphi_0 f(\mathbf{F},\mathbf{n})$. Adhering to the general principles of polymer network mechanics (Panyukov, 1990; Obukhov et al., 1994), we assume a power-law relationship

$$\cos\varphi = \cos\left[\varphi_0\left(\mathbf{n}_j\cdot\mathbf{Cn}_j\right)^{\xi}\right] \tag{36}$$

where the exponent ξ characterizes the sensitivity of deformation ratio to crosslinking angle and the initial value of φ is assumed as $\varphi_0 = \pi/4$. It can be found that Eq. (35) satisfies the initial condition and can also degrade to affine deformation mapping at zero crosslinking distance

$$\begin{aligned} &\text{Initial state}: && \lambda_{cj}\left(\bar{d}=1.0,\sqrt{\mathbf{n}_j\cdot\mathbf{Cn}_j}=1\right)=1.0 \\ &\text{Affine mapping}: && \lambda_{cj}\left(\alpha_0=0\right)=\sqrt{\mathbf{n}_j\cdot\mathbf{Cn}_j}, \quad (j=1,2,\ldots,Q) \end{aligned} \tag{37}$$

2.2.4. Constitutive equations

In this section, we deduce the model Cauchy stress σ and evolution equations of the internal variables ($\mathbf{N}$ and d) based on the non-equilibrium constitutive model framework and the free energy. Combining Eqs. (26) and (17), the Cauchy stress is derived as

$$\boldsymbol{\sigma} = nMk_BT\mathbf{F}\sum_j^Q w_j\left[\frac{N_j}{\lambda_{cj}\sqrt{N_0}}\beta\left(\frac{\lambda_{cj}}{N_j}\sqrt{N_0}\right)\mathbf{u}_j\otimes\mathbf{u}_j\right]\mathbf{F}^T + P\mathbf{I} \tag{38}$$

where P emphasizes the material incompressibility. The constitutive model of SCHs differs from the classical microsphere model in the governing parameters of the stress expression, where the stretch ratio λ_{cj} is derived from a non-affine micro-macroscopic transition model that incorporates a non-zero crosslinking distance, and the chain number N_j is itself a state variable dependent on deformation. Substituting Eqs. (26) into (22) gives the evolution equations for the chain Kuhn segments

$$\begin{aligned} &nMk_BT\frac{B}{N_j+C}+nMk_BT\ln\frac{\beta_j}{\sinh\beta_j}+k_S\dot{N}_j+\Pi_N=0, \quad (j=1,2,3,\ldots,Q) \\ &\sum_{j=1}^{Q}N_j-QN_0=0 \end{aligned} \tag{39}$$

Eq. (39) involves directional chain slippage and segment conservation, from which $Q+1$ variables $(N_1, N_2, \ldots, N_Q, \Pi_N)$ can be solved. Furthermore, the crosslinking distance evolution equation can be deduced through integrating Eqs. (26) and (18)

$$k_bTMn\sqrt{N_0}\left[\sum_{j=1}^{Q}\left(\beta_j\left(\frac{\lambda_{cj}}{N_j}\sqrt{N_0}\right)\right)\frac{\partial\lambda_{cj}}{\partial d}\right]w_j+\chi\left(d-d^0\right)=0 \tag{40}$$

The reference configuration of SCHs is defined as their state at the moment of synthesis, in which the polymer chains are not stress-free. This non-zero stress is embedded in Eq. (40), where the first term remains finite at $\lambda_{cj}=1$. Mechanical equilibrium thus dictates that the reference crosslinking distance must exceed its zero-energy value. This result stems from the requirement for mechanical equilibrium at the crosslinks. The non-zero force in a chain must be balanced by forces at the crosslinking point, thereby inducing a deviation of the crosslinking distance from its zero-force equilibrium position. Details are presented in Section 2.2.5.

2.2.5. Algorithm of the constitutive model

A numerical algorithm is employed to implement the constitutive model for capturing and predicting the mechanical response of SCHs. The primary objective of analyzing the macroscopic mechanical behavior of SCHs is to determine the stress state in the current configuration; however, its evaluation via Eq. (38) depends on the prior determination of the internal variables d and $\mathbf{N}$. Normalizing the crosslinking distance d with respect to its reference value d_0 modifies the crosslinking free energy as follows

$$W_c = \frac{1}{2}\bar{\chi}\left(\bar{d} - \bar{d}^0\right)^2 \tag{41}$$

where $\bar{\chi} = \chi d_0^2$, $\bar{d} = d/d_0$ and $\bar{d}^0 = d^0/d_0$. To this end, the variable $\bar{d}$ is first obtained by numerically solving Eq. (40) via the Newton-Raphson iterative method

$$\bar{d}^{s+1}_{n+1} = \bar{d}^{s}_{n+1} - \frac{f'(\bar{d}^{s}_{n+1})}{f''(\bar{d}^{s}_{n+1})} \tag{42}$$

where $n+1$ denotes the current analysis step, and $s, s+1$ represent the previous and current iteration steps within the current analysis step, respectively. The expressions of $f'(\bar{d}) = \partial f/\partial \bar{d}$ and $f''(\bar{d}) = \partial^2 f/\partial \bar{d}^2$ are

$$\begin{aligned} f'(\bar{d}) &= nMk_BT\sqrt{N_0}\left(\sum_{j=1}^{Q}\beta_j\frac{\partial\lambda_{cj}}{\partial\bar{d}}\right)w_j + \bar{\chi}\left(\bar{d} - \bar{d}^0\right) \\ f''(\bar{d}) &= nMk_BT\sqrt{N_0}\left[\sum_{j=1}^{Q}\left(\beta_j'\frac{\sqrt{N_0}}{N_j}\left(\frac{\partial\lambda_{cj}}{\partial\bar{d}}\right)^2 + \beta_j\frac{\partial^2\lambda_{cj}}{\partial\bar{d}^2}\right)w_j\right] + \bar{\chi} \end{aligned} \tag{43}$$

respectively, where the derivative of the inverse langevin function $\beta'(x)$, the first derivative $\partial\lambda_j/\partial\bar{d}$ and the second derivative $\partial^2\lambda_j/\partial\bar{d}^2$ are

$$\begin{aligned} \beta'(x) &= \frac{300 - 520x + 474x^2 - 126x^3 - 7x^4}{(1-x)^2(10+x)^2} \\ \frac{\partial\lambda_{cj}}{\partial d} &= \frac{\alpha_0\left(\alpha_0\bar{d} - \sqrt{\mathbf{n}\cdot\mathbf{Cn}}\cos\varphi\sqrt{1+\alpha_0\cos\theta_0}\right)}{\sqrt{2\alpha_0^2\bar{d}^2 + 4\mathbf{n}\cdot\mathbf{Cn} + 4\mathbf{n}\cdot\mathbf{Cn}\alpha_0\cos\theta_0 - 4\alpha_0\bar{d}\sqrt{\mathbf{n}\cdot\mathbf{Cn}}\cos\varphi\sqrt{1+\alpha_0\cos\theta_0}}} \\ \frac{\partial^2\lambda_{cj}}{\partial\bar{d}^2} &= -\frac{\alpha_0^2(-3+\cos 2\varphi)\left(1+\alpha_0\cos\theta_0\right)\mathbf{n}\cdot\mathbf{Cn}}{2\sqrt{2}\left(\alpha_0^2\bar{d}^2 + 2\mathbf{n}\cdot\mathbf{Cn} + 2\alpha_0\cos\theta_0\mathbf{n}\cdot\mathbf{Cn} - 2\alpha_0\bar{d}\sqrt{\mathbf{n}\cdot\mathbf{Cn}}\cos\varphi\sqrt{1+\alpha_0\cos\theta_0}\right)^{3/2}} \end{aligned} \tag{44}$$

respectively. Furthermore, a numerical algorithm is subsequently introduced to update $\mathbf{N}$, with the scalar iterative residual defined by the following equation

$$R_N = \sum_{j=1}^{Q} N_j - QN_0 \tag{45}$$

The Newton-Raphson secant method is employed to solve for $\mathbf{N}$. The iterative procedure begins by substituting the previous two estimates, Π_N^{k-1} and Π_N^k, into the first equation of Eq. (39). The corresponding values of N_j^{k-1} and N_j^k are then obtained via the bisection method. These values are subsequently substituted into Eq. (45) to compute the residuals R_N^{k-1} and R_N^k. Finally, the update equation for Π_N is applied as follows

$$\left(\Pi_N\right)^{k+1}_{n+1} = \left(\Pi_N\right)^{k}_{n+1} - \left(\frac{(\Pi)^k_{n+1} - (\Pi)^{k-1}_{n+1}}{\left(R_N\right)^k_{n+1} - \left(R_N\right)^{k-1}_{n+1}}\right)\left(R_N\right)^k_{n+1} \tag{46}$$

To ensure the smooth execution of the iterative process, the initial conditions are determined using Eqs. (43) and (39), respectively

$$\begin{aligned} \bar{d}^0(t=0) &= 1 + \frac{nMk_BT\sqrt{N_0}}{\bar{\chi}}\beta\left(\frac{1}{\sqrt{N_0}}\right)\left(\sum_{j=1}^{Q}\left(\frac{\partial\lambda_{cj}}{\partial\bar{d}}\right)_{t=0}\right)w_j \\ \Pi_N(t=0) &= -nMk_BT\frac{B}{N_0+C} - nMk_BT\ln\frac{\beta\left(\frac{1}{\sqrt{N_0}}\right)}{\sinh\beta\left(\frac{1}{\sqrt{N_0}}\right)} \end{aligned} \tag{47}$$

The first equation can accommodate a non-zero chain force in the reference configuration and the second equation guarantees $N_j(t=0) = N_0$ for all directions. Furthermore, within the numerical implementation, initial conditions for each analysis step must be given. This can be accomplished by treating $\bar{d}_n$ and $\mathbf{N}$ as state variables. Their initial iterative values for the current step are inherited from the converged values of the previous step, namely $\bar{d}^1_{n+1} = \bar{d}_n$ and $\mathbf{N}^1_{n+1} = \mathbf{N}_n$.

The stress of the constitutive model can be determined once the iterative procedures for updating both the internal variable $\bar{d}$ and the normal direction tensor $\mathbf{N}$ have achieved convergence. The comprehensive procedure of the numerical algorithm for this

Table 1
Numerical algorithm of the constitutive model.

Input: parameters, current step: $\mathbf{F}_{n+1}$, Δt, last step: $\bar{d}_n$, $(\Pi_N)_n$, $(\mathbf{N})_n$,
Step1: iteratively calculating the current crosslinking distance $\bar{d}_{n+1}$:
1.0: if $s=1$, then $\bar{d}^s_{n+1}=\bar{d}_n$,
1.1: calculating $\lambda_{cj}(j=1,2,3,\ldots,Q)$ through Eq. (35),
1.2: iteratively calculating the current chain stretch $(N_j)_{n+1}$ and $(\Pi_N)_{n+1}$:
1.2.0: If $k=1$, then $(\Pi_N)^{k-1}_{n+1}=(\Pi_N)_n$ and $(\Pi_N)^k_{n+1}=(\Pi_N)_n+\delta$,
1.2.1: calculation $(N_j)^{k-1}_{n+1}$ and $(N_j)^k_{n+1}$ through Eq. (39),
1.2.2: calculation $(R_N)^{k-1}_{n+1}$ and $(R_N)^k_{n+1}$ through Eq. (45),
1.2.3: checking the convergence:
1.2.3.1: If $\left(\left\|(R_N)^k_{n+1}\right\|>tolerance\right)$, then updating $(\Pi_N)^{k+1}_{n+1}$ through Eq. (46),
$(\Pi_N)^k_{n+1}=(\Pi_N)^{k+1}_{n+1}$, $(\Pi_N)^{k-1}_{n+1}=(\Pi_N)^k_{n+1}$, $k=k+1$, goto step 1.3.0,
1.2.3.2: If $\left(\left\|(R_N)^k_{n+1}\right\|\le tolerance\right)$, then $(\Pi_N)_{n+1}=(\Pi_N)^k_{n+1}$, $\mathbf{N}_{n+1}=\mathbf{N}^k_{n+1}$, goto step 1.4,
1.3: updating $\bar{d}^{s+1}_{n+1}$ through Eq. (42),
1.4: checking the convergence:
1.4.1: If $\left(\left\|\bar{d}^{s+1}_{n+1}-\bar{d}^s_{n+1}\right\|>tolerance\right)$, then $\bar{d}^s_n=\bar{d}^s_{n+1}$, $s=s+1$, goto step 1.0,
1.4.2: If $\left(\left\|\bar{d}^{s+1}_{n+1}-\bar{d}^s_{n+1}\right\|\le tolerance\right)$, then $\bar{d}_{n+1}=\bar{d}^{s+1}_{n+1}$, goto step2,
Step2: calculating the Cauchy stress σ_{n+1} through Eq. (38) and the tangent stiffness matrix $\mathbf{C}_{n+1}$,
Output: state variables of current step: $\bar{d}_{n+1}$, $(\Pi_N)_{n+1}$, $(\mathbf{N})_{n+1}$

Table 2
Values of model parameters employed in the finite element simulation.

Parameter	G(MPa)	N_0	k_{S0}(MPa · s)	$\bar{\chi}$(MPa)	α_0	φ_0	ξ
Value	1.0	50	0.1	0.5	0.01	$\pi/4$	0.01

model is outlined in Table 1. We set the number of integration points for the microsphere model to $Q=21$; the corresponding vectors and weights are provided in Appendix B. A parametric study on the influence of the number of integration points is presented in Section 3.4.2. Based on this numerical algorithm, a UMAT subroutine is developed to simulate the deformation behavior of SCH structures.

3. Results and discussions

Section 2 develops a micro-macroscopic constitutive model for spatial confinement hydrogels, formulating two primary mechanisms: directional chain slippage and crosslinking distance evolution. This section provides the model predictions, focusing on the interaction between these two mechanisms and their effects on the macroscopic mechanical response. Specifically, Section 3.1 compares the proposed model with classical frameworks and presents a parametric sensitivity analysis. Section 3.2 elucidates the effect of the directional chain slippage on rate-dependent mechanical behaviors of SCHs. Section 3.3 investigates the mechanical response of SCHs under diverse fundamental deformation modes, while Section 3.4 discusses the impacts of the free energy approximation, the number of integration points, the coupling between directional chain slippage and the evolution of crosslinking distance and the underlying micro-macroscopic framework.

3.1. SCHs mechanical performance analysis

3.1.1. Modeling predictions

To characterize the proposed model, we first distinguish its theoretical framework from the classical microsphere model, followed by a parametric sensitivity analysis. Finite element simulations were performed under plane strain uniaxial tension. The computational domain (30mm × 15mm) was discretized using 5000 CPE8R elements with reduced integration. Regarding boundary conditions, the left edge was fully constrained, while the right edge was subjected to a prescribed displacement of 180mm at a constant strain rate of $0.6s^{-1}$. We now evaluate the order of magnitude of constitutive model parameters. k_{S0} is a phenomenological parameter used to characterize the macroscopic dissipative behavior of SCHs. Considering that the microscopic mechanism of segment slippage is similar to that of chain entanglement, and based on the study of entanglement relaxation time (Zhong et al., 2023), it can be inferred that k_{S0}(MPa · s) ~ G(MPa) (or potentially smaller). The magnitude of the phenomenological parameter $\bar{\chi}$ can be estimated as $\bar{\chi}$(MPa) ~ G(MPa) (or potentially smaller) according to Eq. (40). Furthermore, the initial crosslinking distance ratio, $\bar{d}^0$, is calculated from the first equation of Eq. (47) as $\bar{d}^0 \sim 1-\alpha_0$. Based on MD simulation results, the ratio of the crosslinking distance to the chain length typically ranges from $(10^{-3}, 10^{-1})$, yielding $\bar{d}^0 \sim (0.9, 0.999)$. Material parameters used in the basic simulation are summarized in Table 2 and we have appropriately expanded the parameter range to further explore their influence on the deformation behavior of SCHs in Section 3.1.2. To enforce the nearly-incompressible constraint, a volumetric penalty term $K(J-1)\mathbf{I}$ was introduced into the stress expression, where the bulk modulus K was set to two orders of magnitude higher than the initial shear modulus G, namely $K=100G$.

Fig. 9(a) illustrates the spatial distribution of the stress field and the chain segment density along the principal stretching direction(N_3). The proposed model differs from the classical framework in that the segment number is not a spatial constant but evolves in response to non uniform deformation gradients. The segment distribution aligns with the characteristics of uniaxial tension: it remains homogeneous in the central region but exhibits significant gradients near the boundaries due to edge effects and geometric constraints. The directional distribution of segments over the microsphere unit sphere (Fig. 9(b)) confirms that segment evolution is intrinsically coupled with the local stretch state. Furthermore, owing to the inherent nonlinearity of the system, the rate of segment redistribution accelerates significantly in the large deformation regime. The simultaneous increase and decrease of segment counts across different orientations indicate a redistribution mechanism that preserves the global conservation of segments. These findings demonstrate that directional chain slippage enables the adaptive segment distribution characteristic of spatial confinement hydrogels. Fig. 9(c) compares the stress responses predicted by the proposed SCH model and the classical microsphere model. The discrepancy between the models at large strains arises from the interplay between crosslinking distance evolution and directional chain slippage. The crosslinking distance $\bar{d}$ influences the mechanical response through two pathways: by modulating the non-affine deformation mapping and by regulating constitutive parameters such as the slippage coefficient k_S. In the strain hardening regime, the non-affine mapping effect becomes prominent, inhibiting the rapid stress build-up as chains approach their extensibility limit.

3.1.2. Characteristics of the constitutive model

Based on the simulation results, a sensitivity analysis evaluates the impact of three fundamental parameters on the mechanical response of SCHs: the initial chain slippage friction coefficient k_{S0}, the crosslinking stiffness coefficient $\bar{\chi}$, and the initial crosslinking distance ratio α_0. The investigated values are $k_{S0} = 0.5, 0.1, 0.01$, $\bar{\chi} = 1.0, 0.5, 0.2$ and $\alpha_0 = 0.05, 0.01, 0.001$, respectively.

Fig. 10(a) depicts the evolution of the dimensionless crosslinking distance $\bar{d}$, which exhibits high sensitivity to parameters $\bar{\chi}$ and α_0. The growth of $\bar{d}$ is mainly governed by the initial chain distance and the crosslinking stiffness: specifically, a small α_0 combined with a large $\bar{\chi}$ inhibits this increase, whereas the opposite promotes it. These two distinct mechanical states can be experimentally tuned by adjusting the salt concentration (Wang et al., 2023a). In contrast to the significant influence of $\bar{\chi}$ and α_0, the parameter k_S exerts a negligible effect on the evolution of $\bar{d}$. The model incorporates two dominant deformation mechanisms in spatial confinement hydrogels: at moderate deformations, directional chain slippage dominates, while at large deformations, especially as molecular chains approach their stretching limits, crosslinking distance evolution becomes predominant. The transition between these two mechanisms exhibits slight non-smoothness due to the depletion of Kuhn segment in the 2-direction. The non-negativity constraint on chain segment number slows its rate of change, leading to an increase in crosslinking distance.

Fig. 10(b) and (c) illustrate the segment numbers along the stretch (N_3) and transverse (N_2) directions. Reducing k_{S0} facilitates increased segment recruitment, while higher values reduce slippage. The non-negativity constraint induces an inflection point in the N_2 curve as it approaches zero at large deformations. Notably, the stress reduction mechanism shifts at this inflection point by transitioning from a process initially driven by increasing chain segments to a regime dominated by non-affine mapping resulting from the expansion of crosslinking distances after segment evolution saturation. The evolution rates of both N_2 and N_3 follow a consistent 'slow-fast-slow' pattern. Furthermore, unlike the microscopic model presented in Section 2.1.3, a distinct asymmetry is observed between the N_3 and N_2 distributions. Fig. 10(d) compares the nominal stress-stretch ratio responses across various parameter sets. The curves differ slightly at moderate deformations but diverge significantly at large strains. This divergence is attributed to the fact that these parameters modulate the evolution of chain segments, which becomes the primary determinant of the mechanical response under large strain conditions.

In order to elucidate the mechanism of non-affine deformation mapping as governed by the crosslinking distance, we inhibited chain slippage, thereby maintaining a constant number of chain segments N_0. Finite element simulations were performed using the same geometry, mesh, and boundary conditions as those detailed in Section 3.1.1. All parameters remain consistent with those in Table 2, with the exception of α_0 and $\bar{\chi}$, which are varied to elucidate the influence of the initial crosslinking distance and crosslinking stiffness on the evolution of $\bar{d}$ ($\alpha_0 = 0.001, 0.05, 0.1$ and $\bar{\chi} = 0.01, 0.05, 1.0$). As illustrated in Fig. 11(a), the normalized crosslinking distance $\bar{d}$ exhibits a pronounced dependence on the stretch ratio: it increases gradually at low strains before rising sharply as the deformation approaches the chain extensibility limit. The response is dictated by the initial network topology: increased initial distances and reduced crosslinking stiffnesses collectively promote the increasing of crosslinking distance. The significance of the non-affine deformation assumption is further highlighted by the stress response presented in Fig. 11(b). While the discrepancy between this model and the classical affine model is negligible at moderate strains, it becomes substantial at large deformations, with the most significant divergence occurring as the stretch ratio approaches the molecular chain contour length. The deformation mapping behavior depends on the topology of the SCH network and deformation state. In the moderate deformation regime, the crosslinking distance is negligible and the network response remains nearly affine. In the large deformation regime, the dramatic increase in $\bar{d}$ renders the mapping relationship non-affine. Our results demonstrate that both the increase in chain segments and the evolution of the crosslinking distance contribute to the mechanical response of SCHs at large strains. These two mechanisms act together to reduce network hardening by decreasing the relative chain stretch ratio $\Lambda = \sqrt{N_0}\lambda_c/N$. Specifically, an increase in chain segments lowers Λ by increasing N, while the associated non-affine deformation reduces the effective stretch λ_c.

3.2. Evaluation of the directional chain slippage

This section investigates the effect of directional chain slippage on the mechanical behavior of SCHs. We inhibit the evolution of crosslinking distance in the theoretical model and conduct strain rate-dependent experiments. While model isolation is straightforward, experimental validation requires suppressing crosslinking distance changes, which can be achieved by lowering the initial

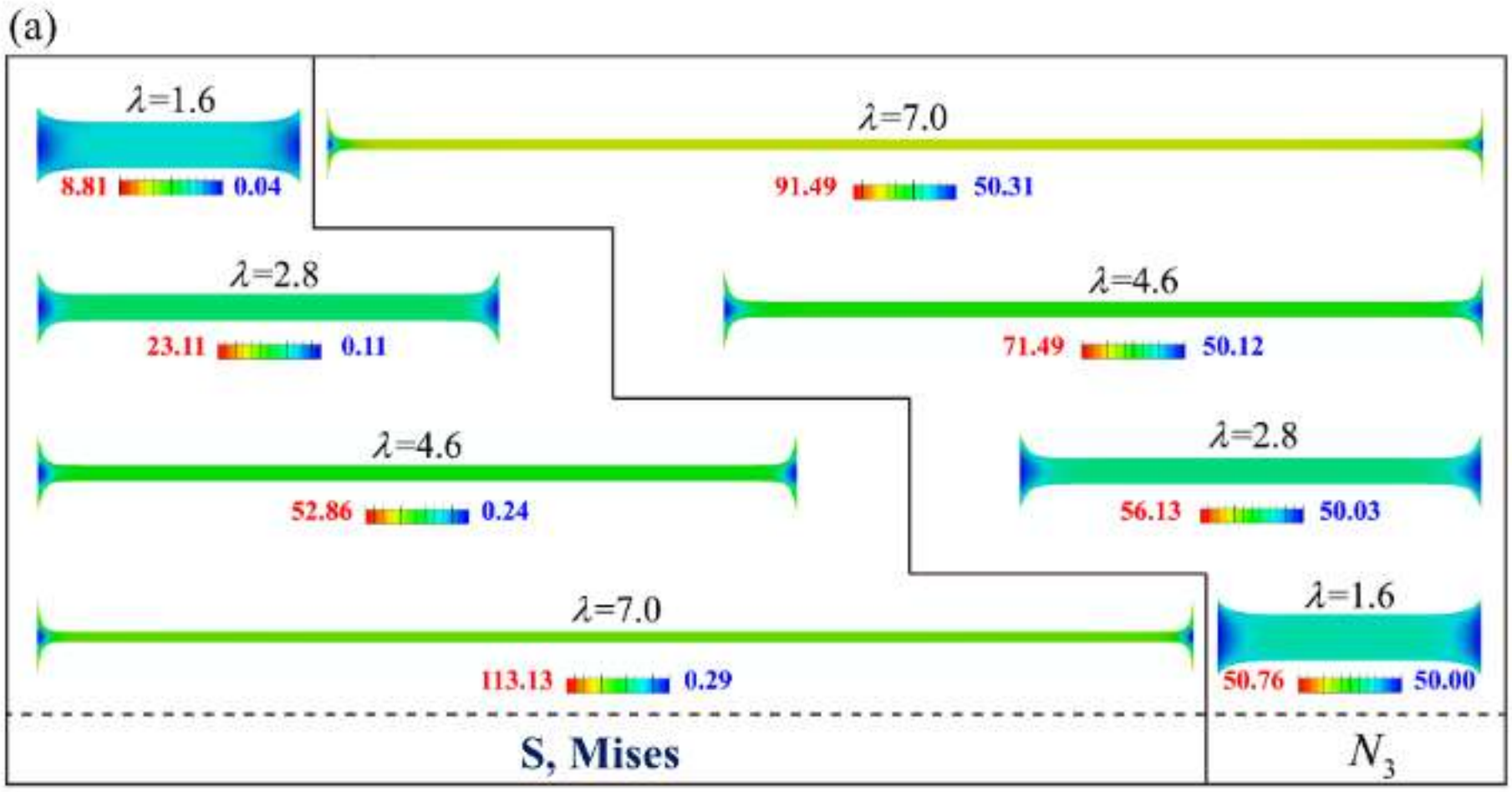

Fig. 9. Performance of SCHs under plane strain uniaxial tension: (a) contours of the Mises stress and the segment along stretch direction N_3, (b) SCHs segments along 21 integration directions as a function of λ, and (c) nominal stress curves as functions of λ from the proposed model and the classical microscopic model.

crosslinking distance ratio and increasing the crosslinking point stiffness. Physically, these conditions are realized by increasing the salt concentration in the hydrogels. Accordingly, we adopt the Acrylamide(AM)-based SCHs reported by Wang et al. (2023a), prepared by dissolving 33g $CaCl_2$, 10.6g AM, and 25mg Irgacure in 50g of water, followed by UV polymerization (365 nm) for 4 h. Obviously, no crosslinking agent (e.g., N,N-methylene bis-acrylamide, MBA) was added during synthesis. Network formation and solid properties therefore arise from spatial confinement crosslinking, not chemical crosslinking. In spatial confinement crosslinking, repulsive forces between salts and polymer chains confine chain segments to a small distance, creating crosslinking points. This confinement restricts but does not fully constrain chain mobility. Molecular chains retain tangential and normal degrees of freedoms, allowing them to slide and alter their segment number. In chemical crosslinking, crosslinking agents permanently join chain ends and eliminate relative chain movement.

3.2.1. Uniaxial tension under various strain rates

In conventional chemical crosslinking hydrogels, the fixed covalent bonds and negligible chain friction render the stress-strain response largely rate-independent (Hassan et al., 2022). In contrast, the rate-dependent mechanical behavior of SCHs, particularly

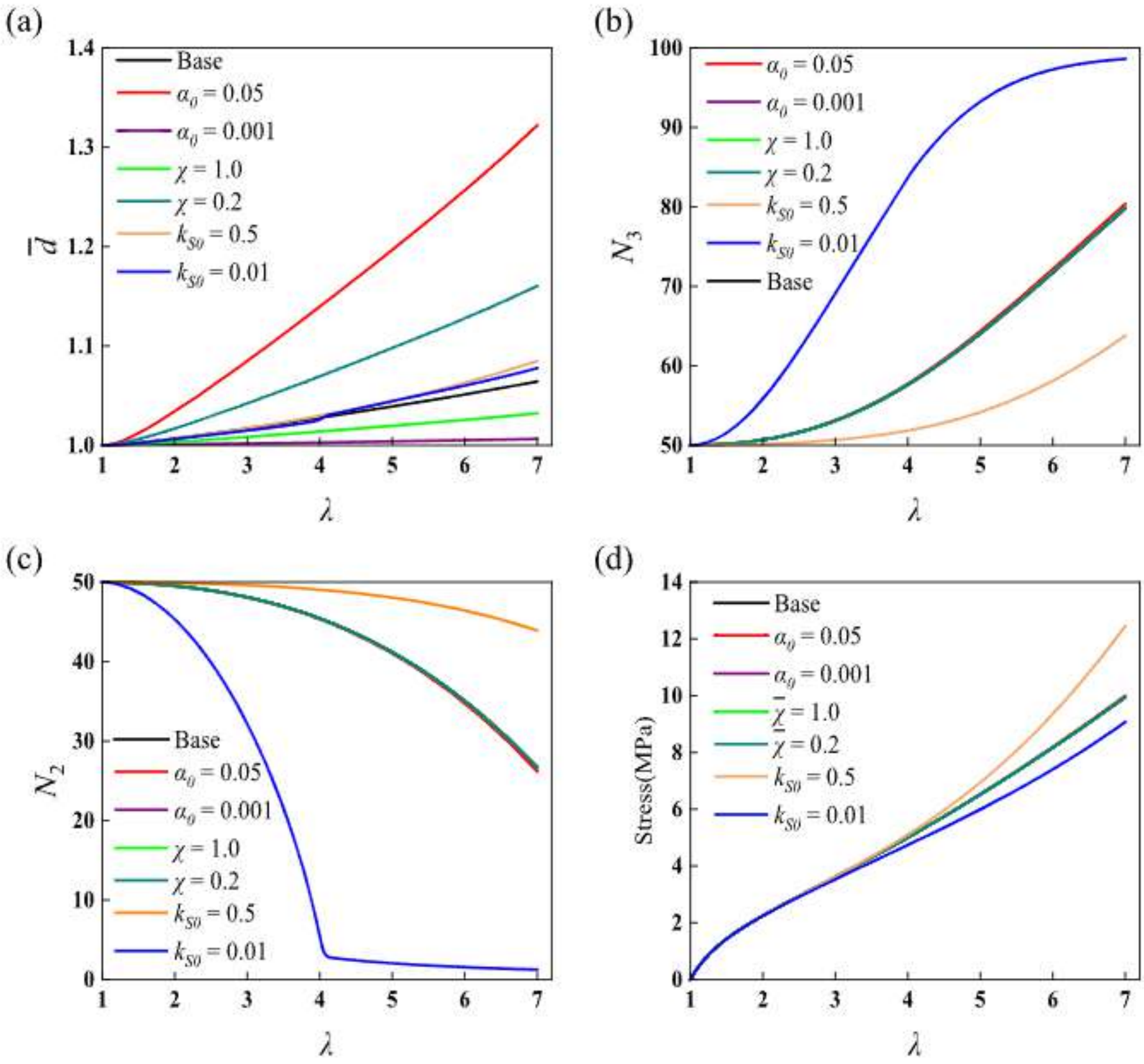

Fig. 10. Results of the parametric sensitivity analysis: (a) the dimensionless crosslinking distance $\bar{d}$, (b)-(c) segments along the stretch direction N_3 and its vertical direction N_2, and (d) the nominal stress. 'Base' represents the finite element simulation in Section 3.1.1.

under large deformations, remains less explored. To address this, we performed uniaxial tension tests on strip specimens (50mm × 15mm × 3mm, with a 30mm gauge length) using a SHIMADZU AGS-X-10KN tester at strain rates of $0.011s^{-1}$, $0.056s^{-1}$, $0.111s^{-1}$, $0.167s^{-1}$, and $0.222s^{-1}$. We then evaluated the constitutive model by comparing numerical predictions with these experimental results. Parameters were identified using the extreme strain rates ($0.011s^{-1}$ and $0.222s^{-1}$), yielding a shear modulus $G = 0.008$MPa, an initial segment number $N_0 = 85$, and a slippage friction coefficient $k_S = 0.00344\text{MPa} \cdot \text{s}$. Based on these parameters, the chain slippage relaxation time is determined to be $\tau \sim k_S/G = 0.43$s. This value is close to the relaxation time of entangled free chains $\tau_e = 0.99$s (Zhong et al., 2023). This similarity arises because chain slippage and entanglement share similar physical mechanisms. The slightly shorter chain slippage relaxation time here is due to the higher water content and lower chain density in SCH network. In the simulation, the sample was discretized into 2700 C3D20R elements. One end of the model was fixed, and the other end was stretched to 195mm in length. The mechanical response of the model was evaluated under identical deformation rates as those in the experiments.

Fig. 12(a) compares the experimental and simulated uniaxial tensile responses, confirming that the model accurately captures the rate sensitivity of SCHs. Notably, the strain-rate effect is negligible at moderate strains but becomes pronounced at larger deformations. Unlike the rate-independent nature of standard hyperelastic hydrogels or classical viscoelasticity, the rate-dependent response of SCHs is governed by the state of deformation. This represents a phenomenological transition in constitutive behavior from hyperelastic dominance to viscoelastic dominance. We attribute this to the fact that chain slippage primarily modulates the effective segment

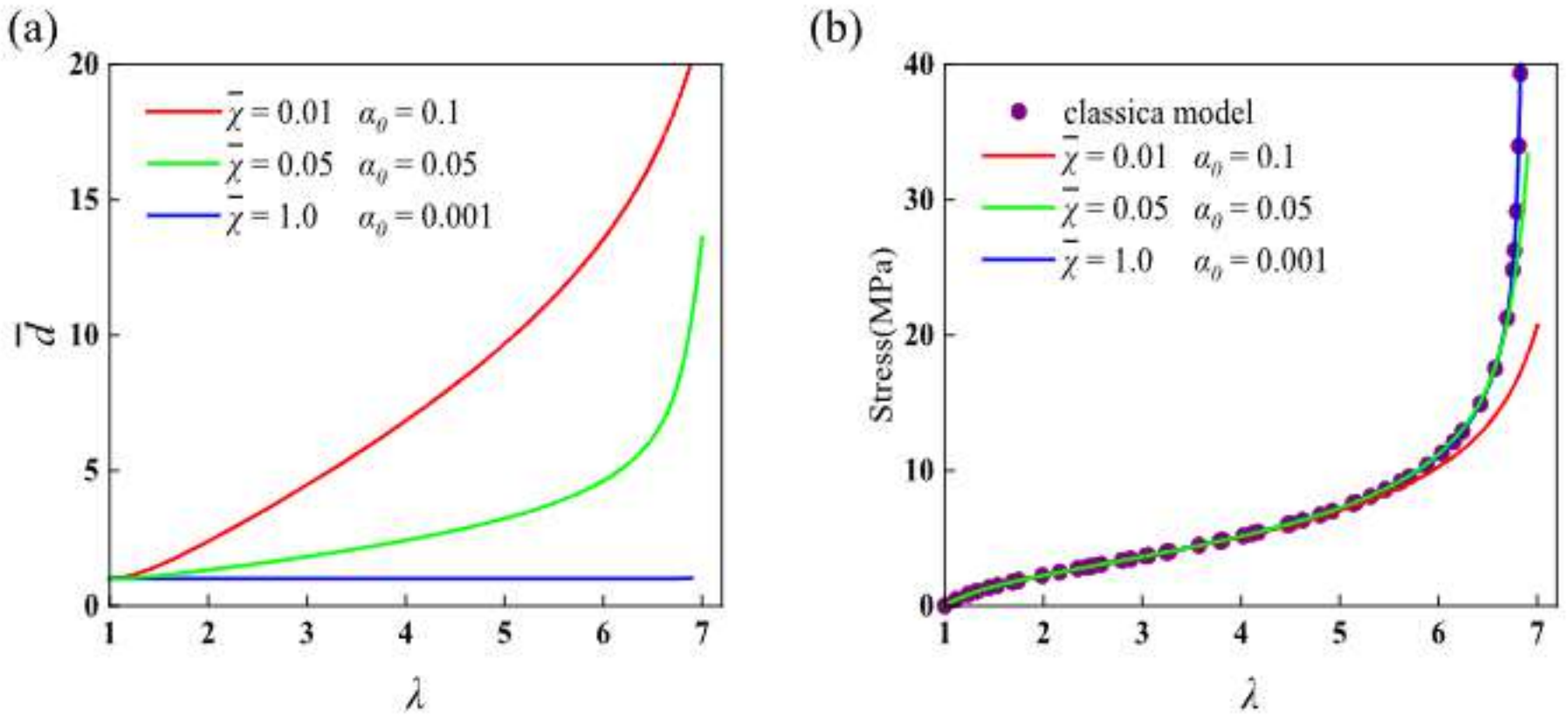

Fig. 11. Results of the non-affine deformation mapping: (a) $\bar{d} - \lambda$ and (b) the nominal stress vs. the stretch ratio λ.

density, with minimal impact on the initial modulus. Importantly, this strain mediated rate sensitivity differentiates our model from several classical and contemporary frameworks, including the rubbery visco-hyperelastic model (Miehe and Göktepe, 2005), the dynamic bond model (Lin et al., 2020), the Gaussian slide-ring model (Vernerey and Lamont, 2021), and the coupled segment slippage model (Liu et al., 2025).

Fig. 12(b) visualizes the evolution of chain segments along unit vectors, showing a transition in the distribution of segment end-points from an initial sphere to an ellipsoid elongated along the loading axis, which indicates directional chain slippage. The unique mechanical response of SCHs is rooted in this deformation state governed by the redistribution of chain segments. Fig. 12(c) and (d) illustrate the evolution of segment numbers N_3 and N_2, respectively, exhibiting a consistent trend across all strain rates: N_3 increases while N_2 decreases. At lower strain rates, the loading duration approaches the chain relaxation time, facilitating more extensive molecular rearrangement and more pronounced stress relaxation. Throughout the deformation, N evolves continuously but has negligible influence on the macroscopic stress at moderate strains, becoming significant at larger deformations.

3.2.2. Simulations of the relaxation process

Relaxation tests are effective for investigating the rate-dependent mechanical properties of materials, as they allow for a clear observation of stress evolution over time. We conducted relaxation experiments on spatial confinement hydrogels using samples identical to those used in the uniaxial tensile tests. One step loading was applied with a displacement of 180mm at four different strain rates: 0.056, 0.222, 0.167 and $0.278s^{-1}$. To replicate these conditions, a finite element model (30mm × 15mm × 3mm) was developed and meshed with 2700 C3D20R elements. The simulation comprised loading (Step 1) and relaxation (Step 2). As shown in Fig. 13(a), the model can capture the characteristic relaxation behavior of SCHs, showing well agreement with experimental data. Fig. 13(b) illustrates the evolution of Kuhn segment numbers in the stretching (N_3) and transverse (N_2) directions. Unlike traditional viscoelastic theories, the relaxation in our model stems from the slippage induced redistribution of Kuhn segments. Since the segment number primarily governs the mechanical response at large strains, the resulting relaxation is less apparent at small strains but becomes progressively more pronounced as the strain increases. This highlights the strain-dependent nature of relaxation in SCHs.

3.3. Response of SCHs under other fundamental deformation modes

3.3.1. Simulation of the plane biaxial tension

Our previous uniaxial tension study identified directional chain slippage and crosslinking distance evolution in SCHs, yet the mechanical response under other deformation modes remains unexplored. Understanding these responses is necessary to accurately predict behavior of SCHs under complex loading conditions. To address this, we first examine the planar biaxial tension response of the material (Fig. 14). The numerical model is discretized using 5268 second-order 2D CPE8R hybrid elements to ensure convergence and prevent shear locking. Regarding the boundary conditions, the bottom and left edges are constrained in their respective normal directions, while a displacement of U =140mm is prescribed along the top and right edges to induce biaxial loading. All relevant material parameters are tabulated in Table 2. Notably, the coupling between the chain slippage friction coefficient and the crosslinking distance is incorporated via Eq. (51), with specific material constants set at $\beta = 20$ and $\bar{d}_{cri} = 3.0$. Finally, to validate the predictive capabilities of our framework, comparative simulations are performed using the classical microsphere model, employing parameters $G = 1$, $N_0 = 50$ and $K = 100G$.

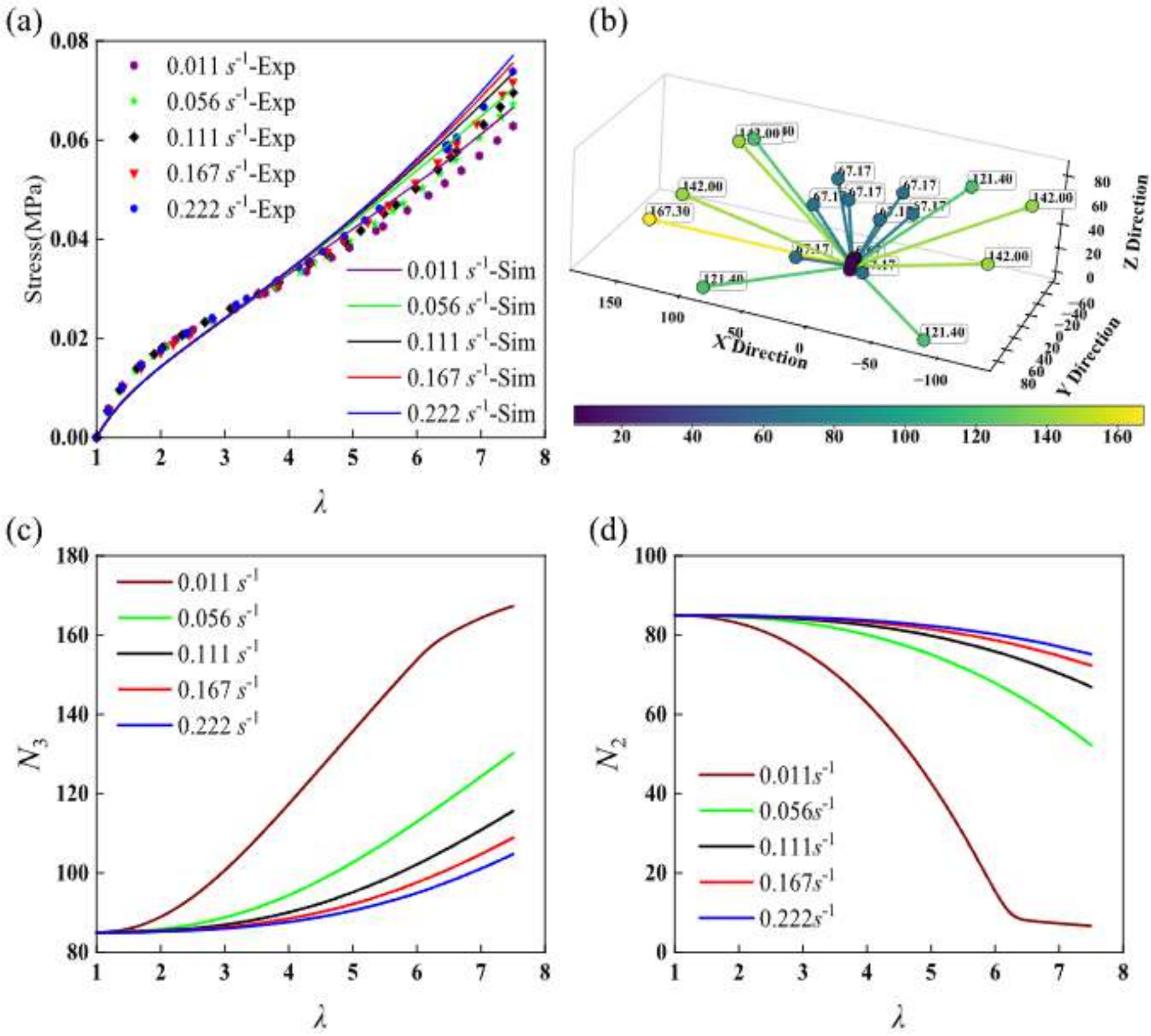

Fig. 12. Results of the SCHs model illustrating directional chain slippage: (a) comparisons of nominal stress between the model predictions and experiments as a function of stretch ratio λ; (b) spatial distribution of chain segments, where the segment vector is defined by the orientation at the 21 integration points Appendix B, with its magnitude given by $N_j (j = 1, 2, \ldots, 21)$; (c)-(d) segment distributions along the stretching direction N_3 and its transverse direction N_2, respectively. Note that the transverse direction can also be denoted as $1 - st$ direction, since $N_1 = N_2$ under 3D uniaxial tension.

Fig. 15 displays snapshots for the Mises stress, the dimensionless crosslinking distance $\bar{d}$ (SDV26), the chain slippage friction coefficient k_S (SDV28), and the number of chain segments along specific directions SDV j (where j corresponds to the unit vector directions specified in Appendix B). These visualizations depict the spatial evolution of the chain segment distribution across various orientations within the material. At the geometric center of the specimen, the structure is subjected to a state of plane equi-biaxial tension. Despite the non-uniform orientation of chain segments (N_j) observed throughout the structure, the incompressibility constraint forces the local deformation state to satisfy $\lambda_1 = \lambda_2 = \lambda_3 = 1.0$ at the center point. The number of chain segments remains constant at its initial value N_0, confirming that directional chain slippage is a direct result of non-equivalent deformation. Under homogeneous deformation modes such as isotropic expansion or free swelling, such directional slippage is suppressed. The mechanical disparity between the proposed SCHs and classical chemically crosslinked hydrogels is primarily dictated by the evolution of the crosslinking distance. Fig. 16 provides a direct comparison of the stress responses at the geometric center for both models; it is evident that the two models diverge significantly as the deformation increases, highlighting the importance of capturing chain slippage and crosslinking distance evolution in the large deformation regime.

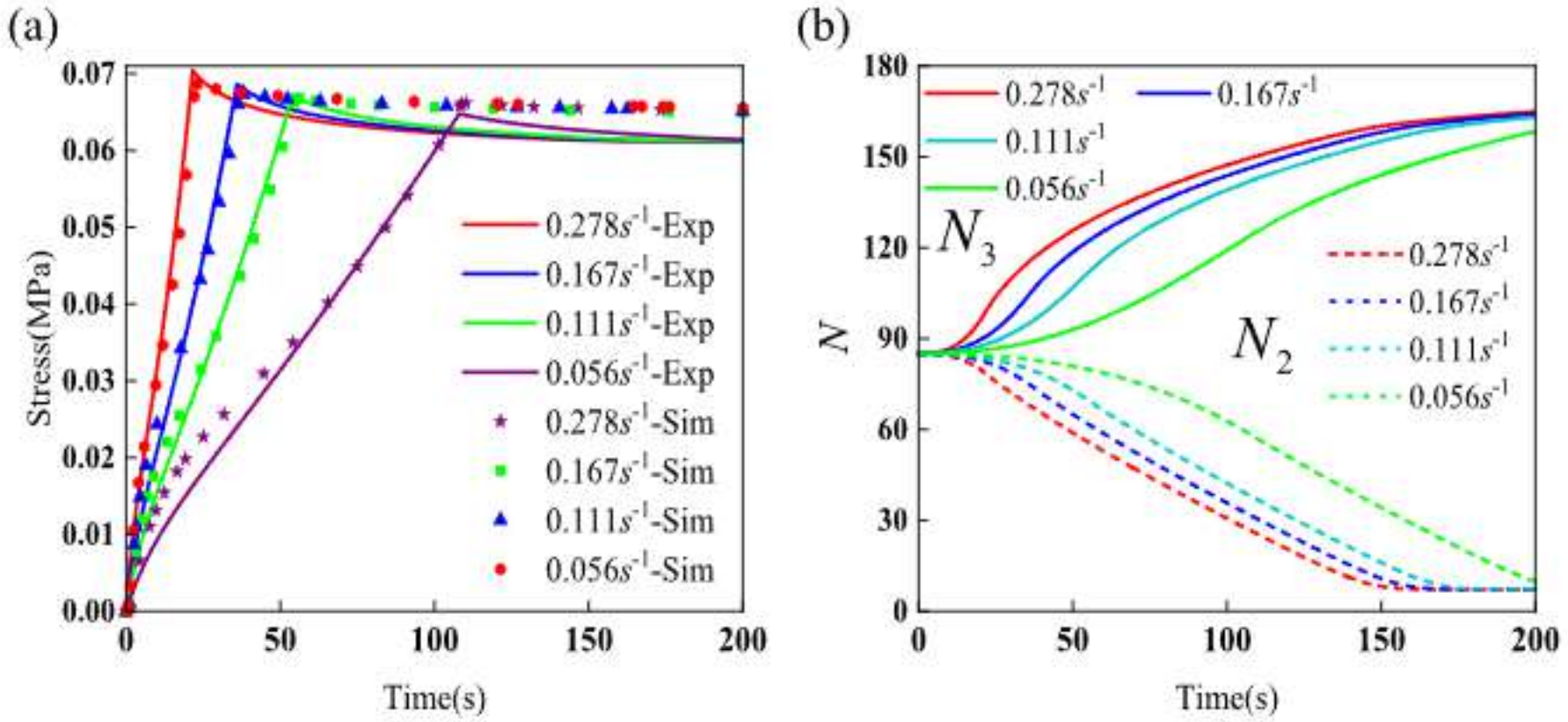

Fig. 13. Relaxation results of SCHs under uniaxial tension: (a) the nominal stress as a function of time and (b) N_3, N_2 as functions of time.

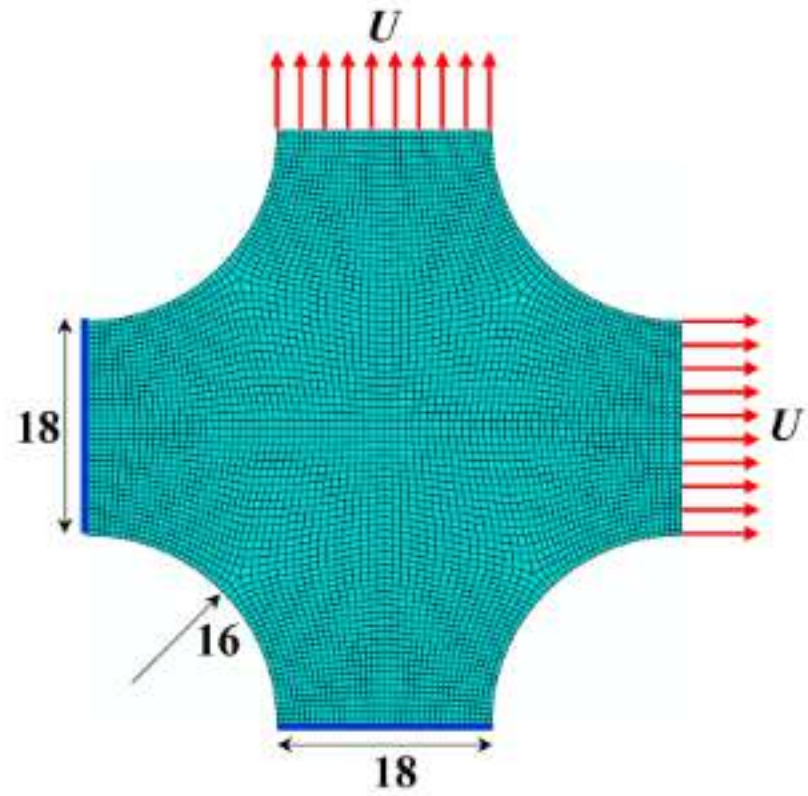

Fig. 14. Prescribed conditions for the plane biaxial tension of SCHs.

3.3.2. *Uniaxial tension of a plate with an elliptical hole*

We preliminarily investigate the toughening mechanisms of SCHs by simulating the deformation of a plate containing an elliptical hole. The geometry and discretization are illustrated in Fig. 17(a). The model is discretized using 27,808 CPE8R elements, with local mesh refinement applied in the vicinity of the elliptical hole to capture the localized stress concentration. Boundary conditions consist of a fully fixed constraint at the bottom edge and a prescribed displacement of $U = 33$mm applied at the top edge. All material parameters are consistent with those in Section 3.3.1. For comparison, an identical simulation is performed using the classical microsphere model. Notably, under the same displacement, the two models exhibit substantially different stress states despite similar macroscopic deformation geometries (Fig. 17(b)). As shown in Fig. 17(c), the SCH model predicts a non-uniform redistribution of chain segments compared to the classical model. Specifically, a higher segment density is observed at the tips of the elliptical major axis, the regions prone to crack initiation. This redistribution enhances the material's resistance to crack propagation, as shown by the stress results in Fig. 17(d). Furthermore, the rearrangement of chain segments increases the effective contour length of the polymer chains, thereby contributing to higher elongation at break.

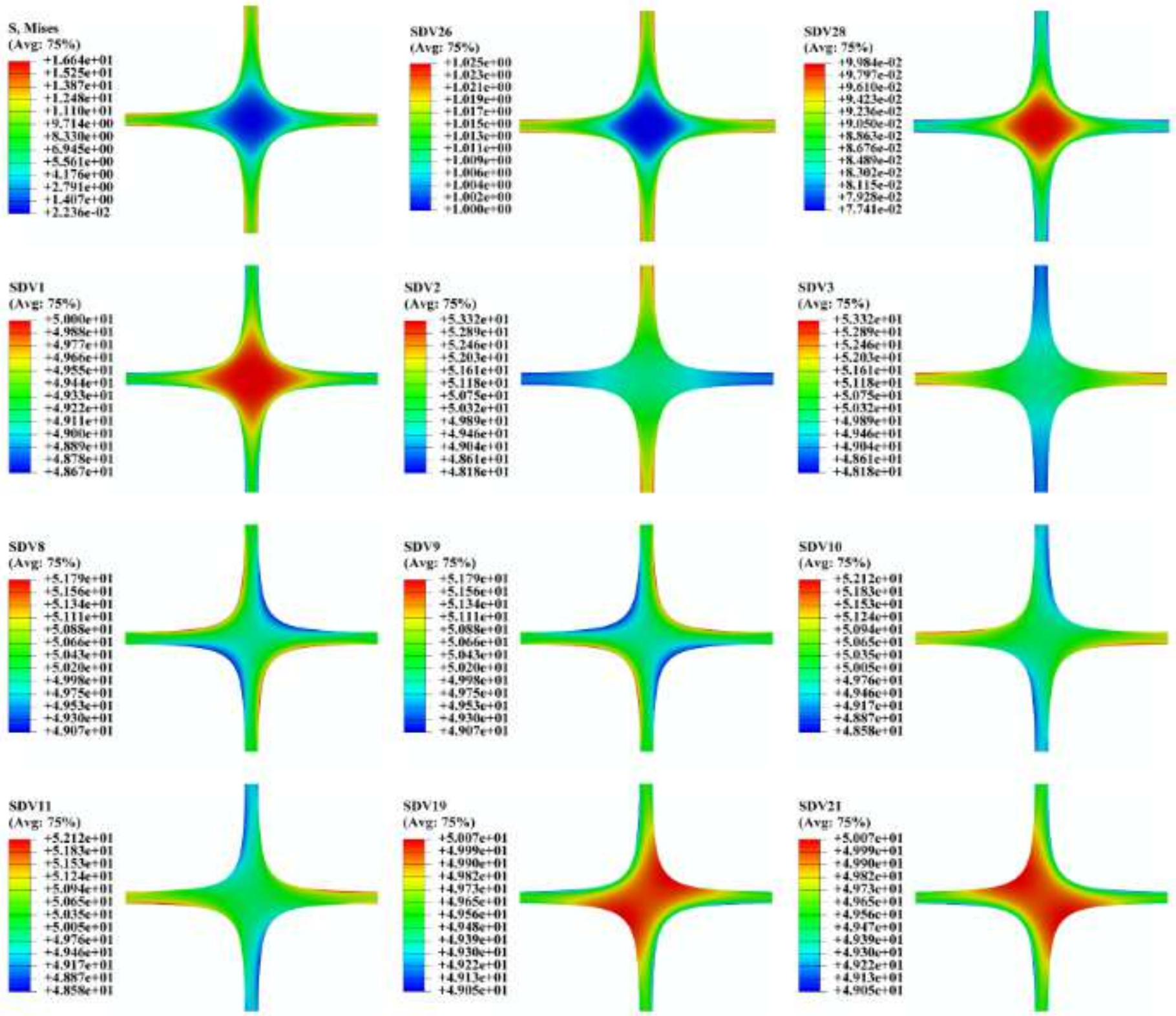

Fig. 15. Snapshots of SCHs upon the plane biaxial tension ($\lambda = 2$). The first 21 state variables (SDV1-SDV21) represent the number of segments in 21 integration directions in the order defined in Appendix B, with SDV26 representing $\bar{d}$ and SDV28 representing k_S. To ensure a clear visualization of the distribution, a cloud plot at a displacement of U =52.23mm is shown. This is because at the maximum calculated displacement of U =140mm, the severe narrowing of the arms renders a distribution contour with poor visual effect.

3.4. Discussions

In this study, we propose a micro-macroscopic constitutive model for spatial confinement hydrogels to elucidate two fundamental mechanisms: directional chain slippage and the evolution of crosslinking distance. Our model incorporates a single-chain free energy function that accounts for chain segment variations within a microsphere-based framework, which captures non-affine deformation through an evolving crosslinking distance. Accordingly, we formulate the free energy for SCH, which consists of two distinct contributions: the elastic energy associated with the polymer chains and the energy related to the crosslinking points. By applying the thermodynamic framework, we derive the evolution equations for the number of chain segments and the crosslinking distance. This constitutive law is implemented via a user-defined material subroutine (UMAT) for finite element analysis. Through multi-mode deformation simulations and parametric studies, we quantify the distinct contributions of chain slippage and crosslinking evolution to the macroscopic mechanical response of SCHs. Finally, the model's predictive accuracy is validated against experimental data, demonstrating its capability to capture strain-rate-dependent behavior.

By adopting some assumptions, including the functional form of the crosslinking free energy Eq. (25)), the geometric assumptions concerning the crosslinking point angles (Eq. (36)), and the estimation of parameters governing crosslinking distance evolution (Table 2), we provide preliminary mechanistic insights into evolution of the crosslinking distance. Nevertheless, as the precise functional expressions and parameter values remain subject to calibration and validation, the current model retains certain limitations. Future studies will integrate molecular dynamics simulations, fluorescence imaging, and degradation experiments to achieve a more nu-

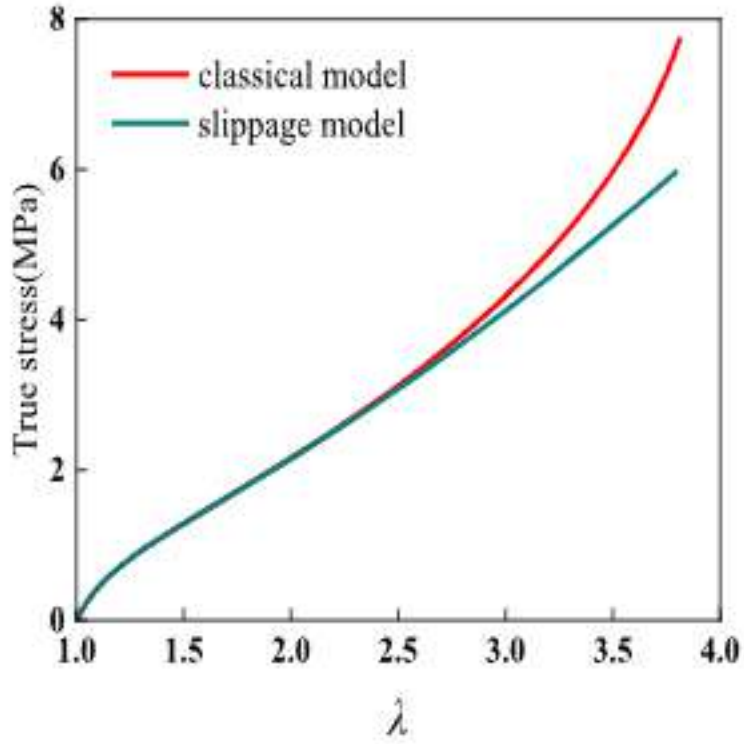

Fig. 16. Comparison of true stress at the geometric center versus structural stretch ratio for the SCHs under plane biaxial tension, as obtained from the slippage model and the classical model.

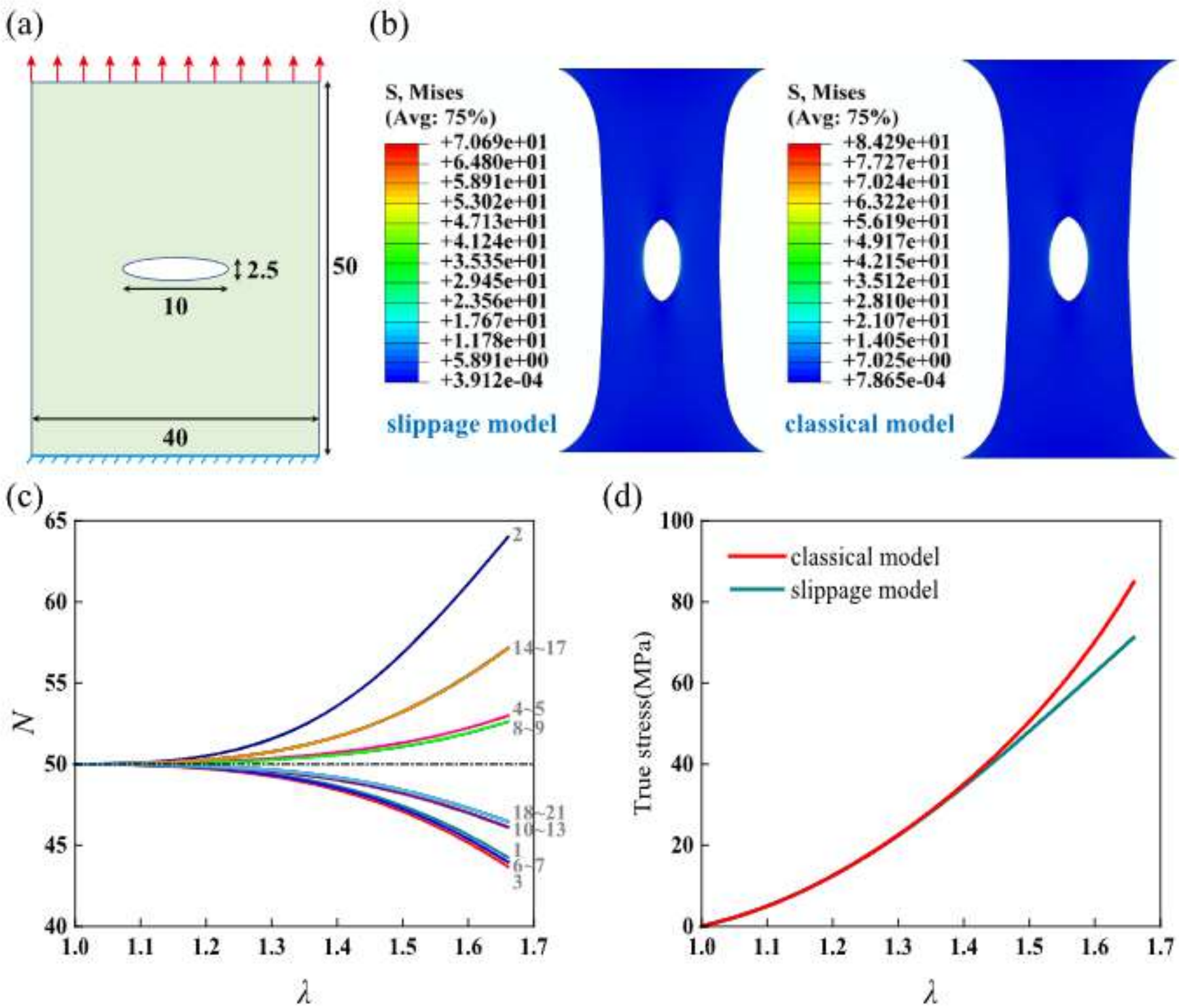

Fig. 17. Uniaxial tension of a plate with an elliptical hole: (a) geometry and boundary conditions, (b) stress contours from the slippage model and the classical model, (c) **N** vs. structural stretch ratio λ, and (d) true stress vs. structural stretch ratio λ.

anced characterization of crosslinking stiffness and its associated energy density. We anticipate that this foundational framework will serve as a robust basis for exploring complex multiphysics coupling behaviors in SCHs, including necking phenomena, self-healing mechanisms, and swelling-induced degradation.

3.4.1. Evaluation of the free energy approximation functions

As shown in Appendix A, regarding the free energy contribution from chain segment variations, we first adopted a fundamental approximation

$$\Xi(N) \sim \ln C_0(b) + \frac{3}{2}\ln(N) \tag{48}$$

This function is further generalized as the expression presented in Eq. (A.10). We then examine the influence of the form of $\Xi(N)$ on the chain slippage behavior and the resulting mechanical response of the SCHs. The derivative of this fundamental approximation with respect to N is given by

$$\frac{\partial \Xi(N)}{\partial N} = \frac{3}{2N} \tag{49}$$

We evaluate the effect of the approximation expression of $\Xi(N)$ from three aspects: the function itself, the microscopic chain system, and the macroscopic mechanical behavior of SCHs. The relative discrepancy (RD) between Eqs. (8) and (49) is defined as

$$e = \frac{\text{Value (Eq. 8)} - \text{Value(Eq. 49)}}{\text{Value(Eq. 49)}} \times 100\,\% \tag{50}$$

Fig. 18(a) compares the curves of $\partial\Xi/\partial N$ derived from Eqs. (8) and (49). A significant relative discrepancy is observed for small N values (specifically $N \leq 20$); however, as N increases, this discrepancy rapidly converges to $\sim 1\,\%$. This feature is further corroborated by Fig. 18(b), based on Eq. (10) with $N_0 = 100$. Consequently, for sufficiently large N , the influence of chain stretch on slippage can be accurately captured by Eq. (49), even in large deformation regimes. To further evaluate the impact of different approximations of $\Xi(N)$ on the deformation behavior of microscopic chain systems, we utilize the rectangular loop model established in Section 2.1.3. The comparison results (Fig. 18(c) and (d)) reveal that the relative discrepancy varies monotonically for N_1, f_1 and f_2, but shows non-monotonic behavior for N_2. This suggests a competitive mechanism between the chain segment evolution and the stretch ratio. Specifically, increasing the segment number or decreasing the stretch ratio generally reduces the discrepancy. The non-monotonicity observed in N_2 can be attributed to a shift in the dominant mechanism: in the moderate stretch range, the rapid reduction in segment number drives the discrepancy; at higher stretches, the rate of change in N levels off, and the chain stretch becomes the dominant factor, leading to a decrease in the discrepancy. Finally, we assess the influence of $\Xi(N)$ on the macroscopic mechanical properties of SCHs (Fig. 18(e) and (f)). The results demonstrate that compared to the microscopic chain system, the discrepancy in the number of chain segments arising from the approximation function is further reduced. Especially regarding the stress response, this discrepancy is so minor that it can be considered negligible.

Based on the above discussions, both approximations (Eqs. (8) and (49)) are effective in capturing the directional chain slippage and deformation response of both microscopic chain networks and macroscopic hydrogels. The discrepancy between these formulations diminishes significantly by several orders of magnitude when one transitions from the microscopic to the macroscopic scale. Notably, for macroscopic stress-stretch behavior, this discrepancy becomes negligible. Consequently, we recommend Eq. (8) for analyzing microscopic chain systems due to its superior mathematical generality. Conversely, for macroscopic hydrogel mechanics, Eq. (49) is preferred because it eliminates the need for fitting parameters.

3.4.2. Influence of the number of integration points

In above analysis, the microsphere model serves as the micro-to-macro transition framework, with 21 integration points employed to discretize the sphere. To assess whether increasing the number of integration points enhances model accuracy, we simulated uniaxial tension at various strain rates (following Section 3.3.1) using 37 and 61 integration points (Bažant and Oh, 1986; Zhong et al., 2019). As illustrated in Fig. 19(a) and (b), the results of different integration points are relatively close, where the 37-point discretization achieves the best accuracy.

3.4.3. Evolution of chain slippage friction coefficient with crosslinking distance

This section examines the mechanical response of the SCHs by focusing on the coupling between directional chain slippage and the evolution of crosslinking distance. We investigate how the evolution of $\bar{d}$ influences chain slippage, which is governed by the coefficient k_S. The geometry and mesh remain consistent with those in Section 3.1.1. The relationship between $\bar{d}$ and k_S is defined in Eq. (51), with the critical crosslinking distance $\bar{d}_{cri}$ set to 3.0 (Fig. 20(a)). To evaluate the impact of k_S on the stress-strain response, we compare the results against simulations with a constant k_S (Fig. 20(b)). Numerical results demonstrate that chain segment and stress are sensitive to $\bar{d}$. Specifically, an increase in $\bar{d}$ softens the SCHs by increasing the segment; this effect is mediated by the coupling between chain slippage and crosslinking distance evolution. A sensitivity of k_S to $\bar{d}$ accelerates the chain slippage process, thereby amplifying the stress reduction effect, particularly under large deformation.

$$k_S = k_{S0}\exp\left(-\beta\frac{\bar{d}-1.0}{\bar{d}-\bar{d}_{cri}}\right) \tag{51}$$

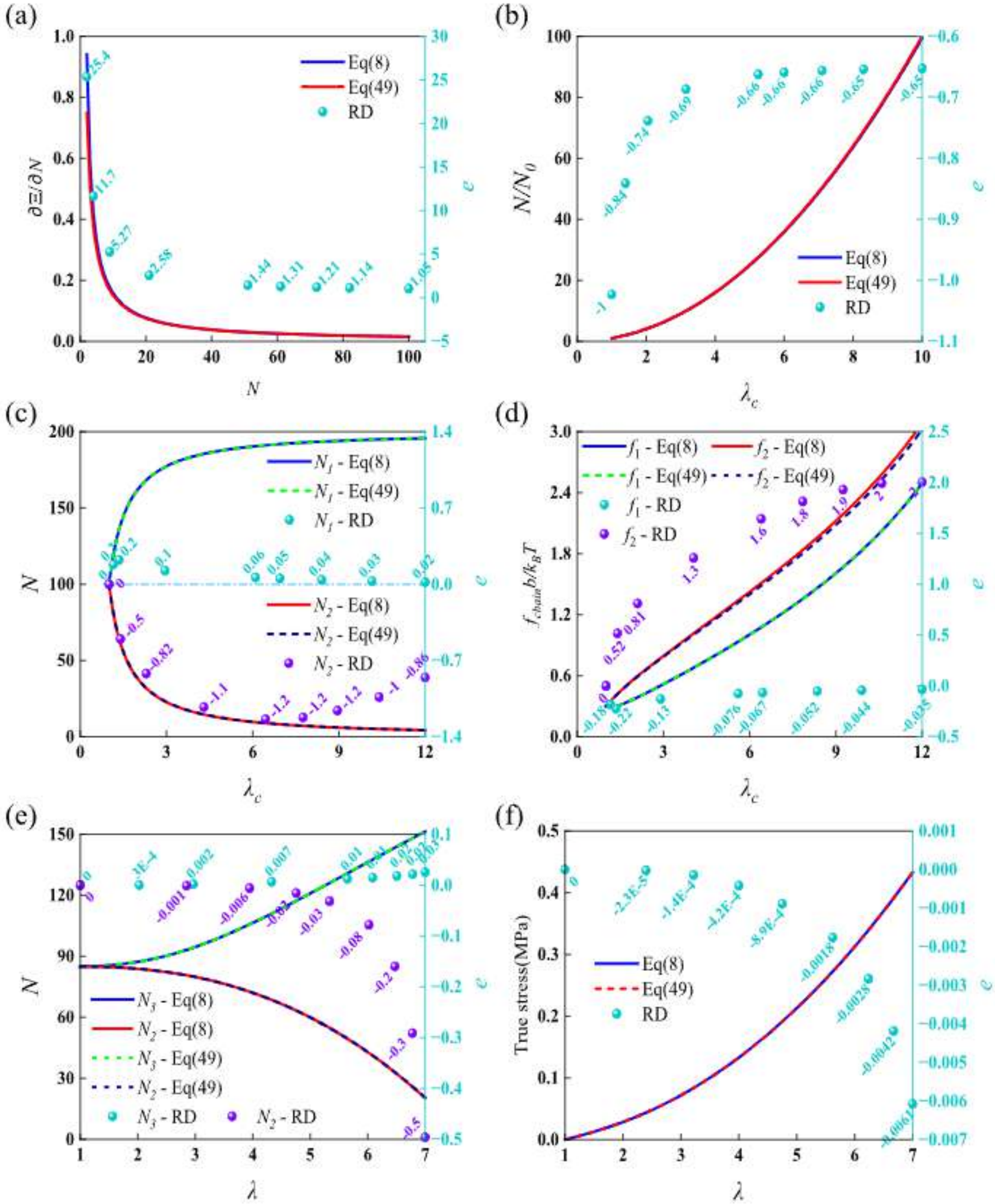

Fig. 18. Evaluation of different $\Xi(N)$ approximations: (a) Curves of Eqs. (8) and (49), (b) N/N_0 versus λ_c derived from Eq. (10), (c)-(d) evolution of chain segments and chain forces for the rectangular loop chain, (e)-(f) evolution of chain segments and stress for SCHs..

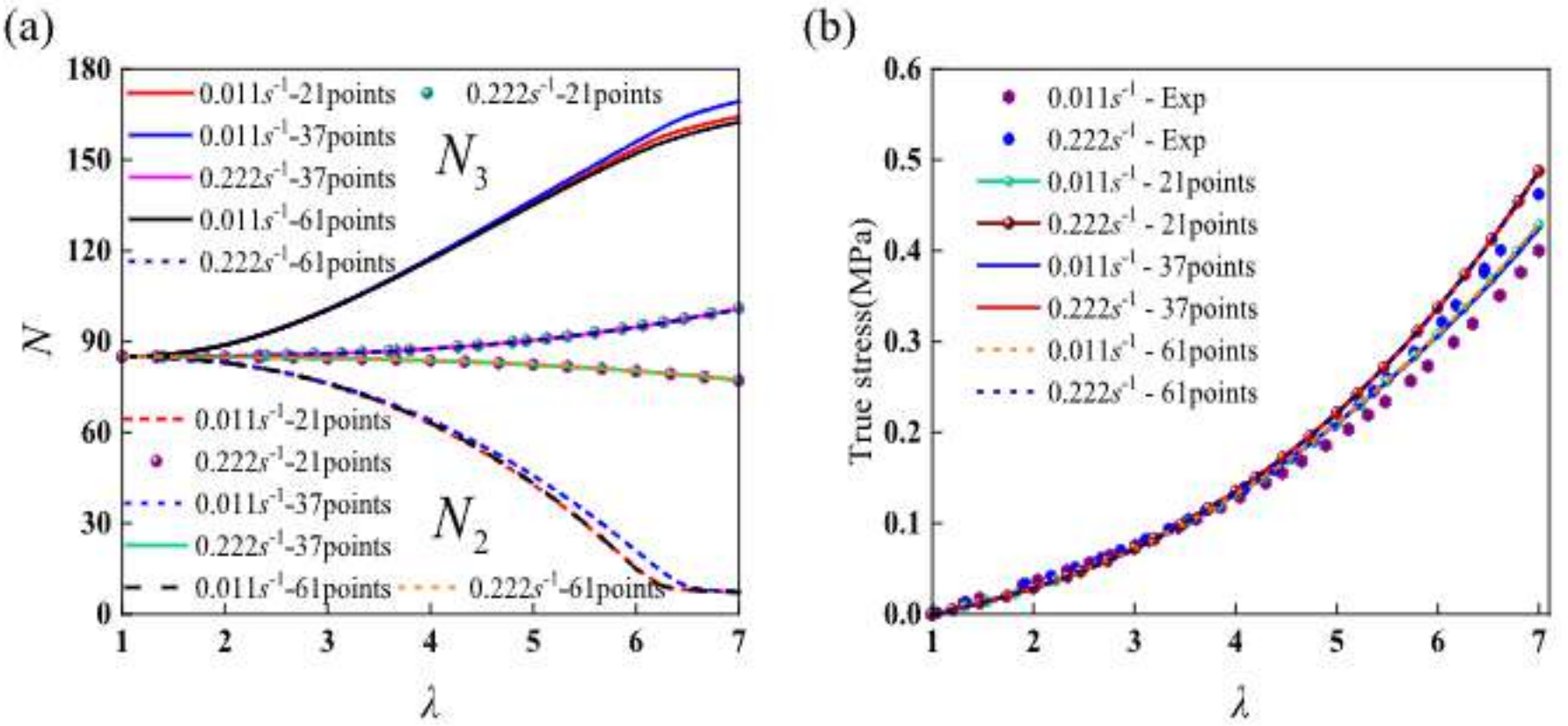

Fig. 19. Comparison of experimental and simulation results for SCHs under uniaxial tension, with simulations using 21, 37, and 61 integration points respectively: (a) chain segment and (b) true stress. .

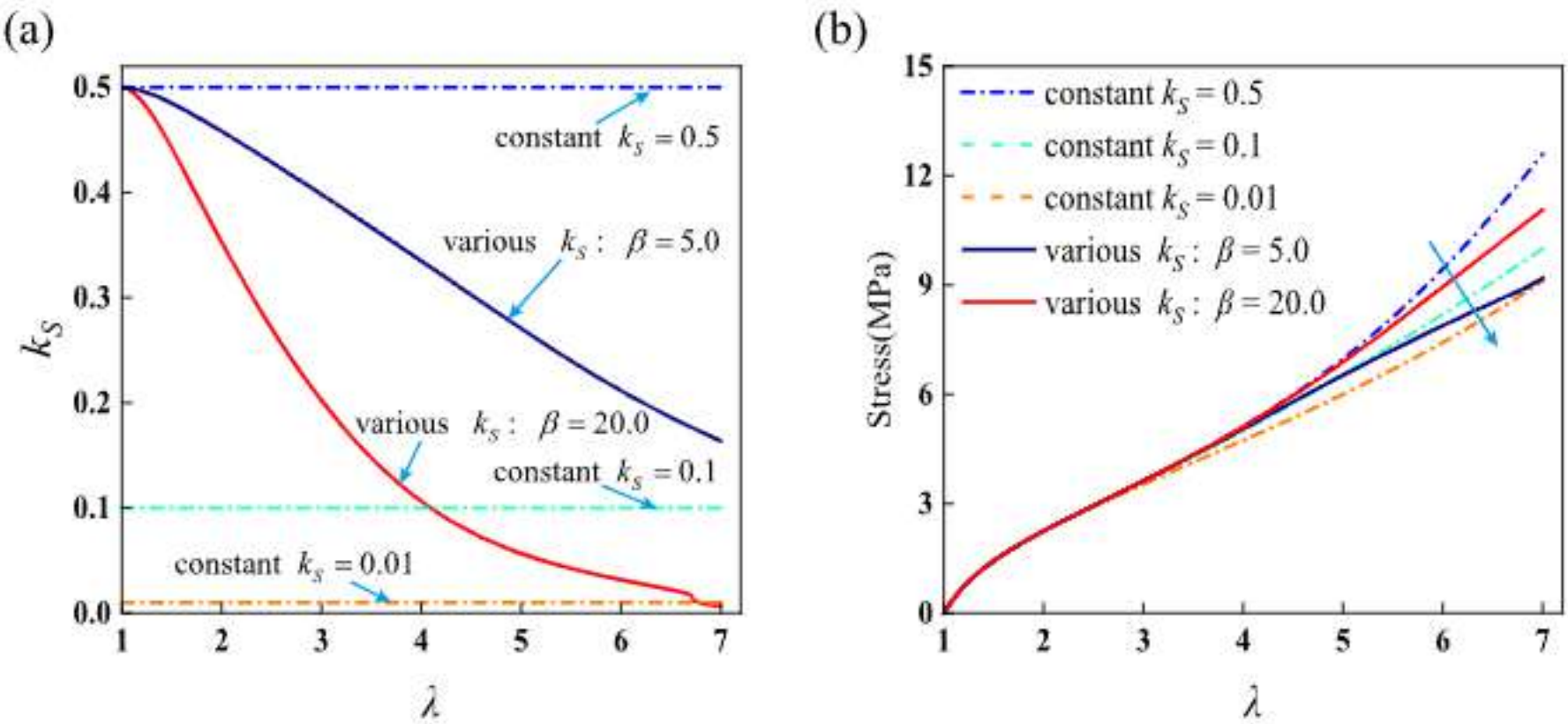

Fig. 20. Simulation results of the SCHs model illustrating the effect of crosslinking distance $\bar{d}$ on the chain slippage friction coefficient k_S: (a) k_S and $\bar{d}$ calculated from Eq. (51), and (b) nominal stress as a function of stretch ratio λ.

3.4.4. Other micro-macroscopic model

Furthermore, to extend our framework beyond the microsphere model, we evaluate alternative constitutive modeling approaches. We implement the classical three chain and eight chain schemes alongside the microsphere model to provide a useful comparison. These represent the most prominent micro-macroscopic frameworks for hydrogel modeling: the three chain model provides an intuitive physical picture with a concise mathematical formulation (Wang and Guth, 1952); the eight chain model retains mathematical simplicity while capturing the spatial distribution of polymer chains (Arruda and Boyce, 1993); and the microsphere model, despite its higher numerical complexity, explicitly accounts for the statistical chain distribution in dense spatial directions (Miehe et al., 2004). While these models have been compared in previous studies (Wu and Van Der Giessen, 1993), their predictive capabilities for spatial confinement networks under large deformations remain unverified. To this end, we adapt the three chain and eight chain models to the context of SCHs and compare the resulting constitutive responses.

■ **Three chain model**

According to its basic physical picture, the chains in the three chain model are uniformly distributed solely along the three principal axes. The Lagrangian function can thus be formulated as

$$L_{3chain}(\mathbf{C},\mathbf{N}) = \frac{nMk_BT}{3}\sum_{j=1}^{3}\left[A + B\ln(N_j + C)\right] + \frac{nMk_BT}{3}\sum_{j=1}^{3}N_j\left(\Lambda_j\beta_j + \ln\frac{\beta_j}{\sinh\beta_j}\right) + \frac{1}{2}\chi\left(d - d^0\right)^2 + \Pi_N\left(\sum_{j=1}^{3}N_j - 3N_0\right) \tag{52}$$

where $\mathbf{N}$ now is defined as $\{N_1, N_2, N_3\}$ and $\beta_j = L^{-1}(\Lambda_j)$. Λ_j is

$$\Lambda_j = \sqrt{N_0}\frac{\lambda_{cj}}{N}$$
$$\lambda_{cj} = \sqrt{\frac{2\lambda_j^2\left(1 + \alpha_0\cos\theta_0\right) + \alpha_0^2\bar{d}^2 - 2\alpha_0\bar{d}\lambda_j\cos\varphi\sqrt{1 + \alpha_0\cos\theta_0}}{2}} \quad (j = 1,2,3) \tag{53}$$

The evolution equation of $\bar{d}$ is

$$\frac{\partial L_{chain}}{\partial\bar{d}} = 0: \quad \frac{nMk_BT}{3}\sqrt{N_0}\sum_{j}^{3}\beta_j\frac{\partial\lambda_{cj}}{\partial\bar{d}} + \bar{\chi}\left(\bar{d} - \bar{d}^0\right) = 0 \tag{54}$$

where

$$\frac{\partial\lambda_{cj}}{\partial\bar{d}} = \frac{\sqrt{2}\left(\alpha_0^2\bar{d} - \alpha_0\lambda_j\cos\varphi\sqrt{1 + \alpha_0\cos\theta_0}\right)}{\sqrt{2\lambda_j^2\left(1 + \alpha_0\cos\theta_0\right) + \alpha_0^2\bar{d}^2 - 2\alpha_0\bar{d}\lambda_j\cos\varphi\sqrt{1 + \alpha_0\cos\theta_0}}} \quad (j = 1,2,3) \tag{55}$$

Similar to the microsphere model, the governing equations of chain slippage are

$$\frac{\partial L_{3chain}}{\partial N_j} = 0: \quad \frac{B}{N_j + C} + \ln\frac{\beta_j}{\sinh\beta_j} + \frac{3k_S}{k_BTMn}\dot{N}_j + \frac{3\Pi_N}{k_BTMn} = 0 \quad (j = 1,2,3)$$
$$\frac{\partial L_{3chain}}{\partial\Pi_N} = 0: \quad \sum_{j}^{3}N_j - 3N_0 = 0 \tag{56}$$

and the principal stress is

$$\sigma_j = \lambda_j\frac{\partial L_{3chain}}{\partial\lambda_j} = \frac{k_BTMn}{3}\beta_j\sqrt{N_0}\lambda_j - P \quad (j = 1,2,3) \tag{57}$$

The three directional chain numbers are solved numerically from Eq. (56), and the principal stresses are subsequently calculated via Eq. (57).

■ Eight chain model

The eight chain model is widely adopted for rubber and hydrogel constitutive modeling due to its intuitive physical interpretation, mathematical simplicity, and inherent frame invariance. However, a fundamental kinematic incompatibility exists between this model and the mechanism of chain slippage. The model assumes a uniform stretch ratio for all chains, which fails to capture the stochastic distribution of chain segments in spatially confined networks. Consequently, the standard eight chain model cannot be directly applied to such systems. To address this, we formulate a modified eight chain model for spatial confinement hydrogels, with its Lagrangian defined as follows:

$$L_{8chain}(\mathbf{C},\mathbf{N}) = \frac{nMk_BT}{3}\sum_{j}^{3}\left[\left(A + B\ln(N_j + C)\right) + N_j\left(\Lambda\beta + \ln\frac{\beta}{\sinh\beta}\right)\right] + \Pi_N\left(\sum_{j=1}^{3}N_j - 3N_0\right),$$
$$\text{and} \quad \Lambda = \sqrt{\frac{N_0}{3}\sum_{j=1}^{3}\frac{\lambda_j^2}{N_j^2}} \tag{58}$$

The incorporation of $\bar{d}$ into the eight chain model remains a challenge and constitutes an important goal for future work. In a similar manner, the governing equations of chain slippage can be obtained through the derivatives of L_{8chain} with respect to N_j and Π_N, respectively

$$\frac{\partial L_{8chain}}{\partial N_j} = 0: \quad \frac{B}{N_j + C} - \frac{N_0^2\beta\lambda_j^2}{\Lambda N_j^3} + \frac{3k_S}{k_BTMn}\dot{N}_j + \frac{3\Pi_N}{k_BTMn} = 0 \quad (j = 1,2,3),$$
$$\frac{\partial L_{8chain}}{\partial\Pi_N} = 0: \quad \sum_{j}^{3}N_j - 3N_0 = 0 \tag{59}$$

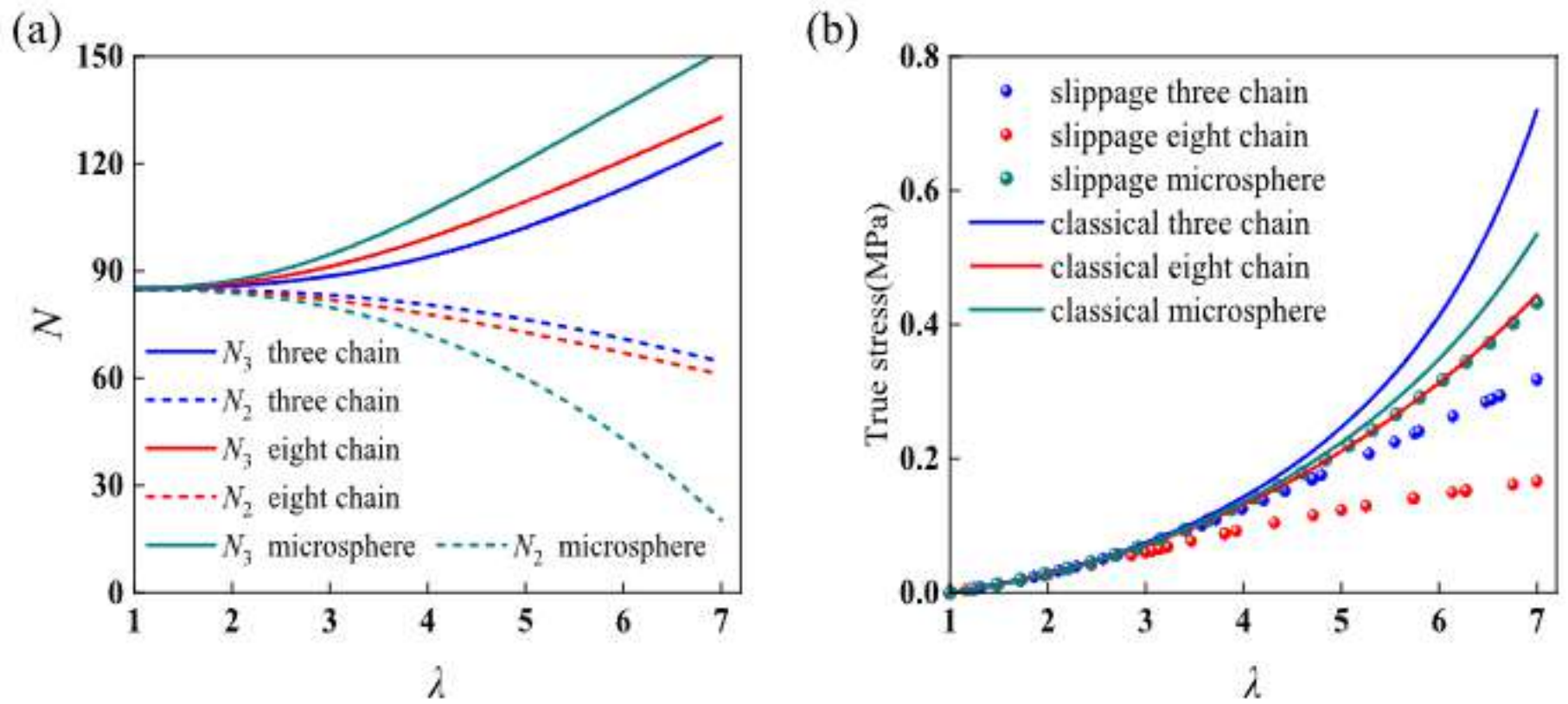

Fig. 21. Comparison of three micro-macro approaches for SCHs: the three chain, eight chain, and microsphere models. Results show (a) the segment evolution law and (b) the true stress as functions of λ, respectively.

The principal stress can be obtained through the derivative of L_{8chain} with respect to λ_j

$$\sigma_j = \lambda_j \frac{\partial W}{\partial \lambda_j} = k_B T M n \frac{\beta N_0^2}{3\Lambda N_j^2} \lambda_j^2 - P \quad (j = 1, 2, 3) \tag{60}$$

To resolve this contradiction between chain slippage and the assumption of identical chain stretch in the eight-chain model, we sacrificed its full tensor form. Consequently, a new constitutive model for SCHs was constructed based on a principal stress formulation. For these three micro-macroscopic models, we performed numerical calculations and evaluated their predictive capabilities for chain slippage. A uniaxial tension deformation mode where $\lambda_3 = \lambda$, $\lambda_1 = \lambda_2 = \lambda^{-0.5}$ is utilized in this section, and parameters are the same as those in Section 3.1.1. Model results are depicted in Fig. 21(a) and (b). All three models can capture the chain slippage behavior, which is a fundamental feature of spatially confined hydrogels. The slippage and classical models exhibit excellent consistency in the intermediate deformation regime, but their predictions diverge substantially under large deformation. At a given strain, the three slippage models not only yield lower stresses than the classical model but also demonstrate a different ordering of stress values relative to each other. This phenomenon is a key feature of the slippage network models, reflecting their direct sensitivity to the count of chain segments.

4. Summary and outlook

In this study, we propose a micro-macroscopic constitutive model for spatial confinement hydrogels, centered on two fundamental mechanisms: directional chain slippage and the evolution of crosslinking distance. The development of this model is rooted in a refined free energy expression for individual polymer chains, which accounts for the variation in the number of Kuhn segments. Our micromechanical analysis demonstrates that the adaptive redistribution of chain segments promotes a more uniform distribution of tensile forces, thereby mitigating the risk of localized chain scission and allowing the network to access a lower energy state compared to conventional chemically crosslinked systems. Building upon this microscopic framework, we developed a continuum model for spatial confinement hydrogels governed by three primary physical variables: (i) the deformation gradient, (ii) the Kuhn segment vector, and (iii) the crosslinking distance. By incorporating a non-affine micro-macroscopic mapping that accounts for finite crosslinking distances, we established the governing equations for both directional chain slippage and crosslink evolution. Numerical results indicate that while these mechanisms have a marginal impact under moderate deformation, they play a critical role in stress relaxation during large deformation regimes. We observed a shift in the dominant mechanism with increasing strain: directional chain slippage prevails initially, while the evolution of crosslinking distances becomes the primary driver as slippage approaches saturation. Furthermore, our model reveals a strain rate-dependent transition in mechanical behavior, characterized by a shift from hyperelastic-dominated to viscoelastic-dominated performance. Notably, the redistribution of chain segments is shown to enhance the fracture toughness of these hydrogels. Given the inherent complexity of spatial confinement hydrogels and the emergent nature of research in this field, this work establishes a foundational network model. This framework provides a basis for investigating advanced phenomena in spatial confinement hydrogels, such as necking, unloading-induced instability, self-healing, and swelling-induced degradation.

CRediT authorship contribution statement

Yunqiang Hu: Writing – original draft, Visualization, Methodology, Formal analysis, Conceptualization; **Zhaoguo Gao:** Visualization, Investigation, Conceptualization; **Fei Jia:** Writing – original draft, Visualization, Methodology, Formal analysis; **Yanju Liu:** Writing – original draft, Supervision; **Jinsong Leng:** Writing – original draft, Supervision, Project administration.

Data availability

Data will be made available on request.

Declaration of competing interest

The authors declare that they have no known competing financial interests or personal relationships that could have appeared to influence the work reported in this paper.

Appendix A. Approximation of the integration function

In classical crosslinking network models, the Kuhn segment number of an individual chain is fixed, $\Xi(N)$ is treated as a constant and its specific form is insignificant. However, in spatial confinement network, the mapping between N and $\Xi(N)$ must be precisely determined. $\Xi(N)$ is defined as

$$\Xi(N) = \ln\left[4\pi \int_0^{Nb} \exp\left(-N\frac{r}{Nb}\beta\left(\frac{r}{Nb}\right) - N\ln\frac{\beta\left(\frac{r}{Nb}\right)}{\sinh\beta\left(\frac{r}{Nb}\right)}\right) r^2 dr\right] \tag{A.1}$$

It can be found that Ξ is a function of N when the single Kuhn segment length b is fixed. While an analytical closed-form solution is intractable, we establish the underlying functional form through mathematical analysis and determine the explicit expression using numerical methods. I is introduced and defined as

$$I = 4\pi \int_0^{Nb} \exp\left(-N\frac{r}{Nb}\beta\left(\frac{r}{Nb}\right) - N\ln\frac{\beta\left(\frac{r}{Nb}\right)}{\sinh\beta\left(\frac{r}{Nb}\right)}\right) r^2 dr \tag{A.2}$$

Additionally, the function S is further introduced as

$$S = \frac{r}{Nb}\beta\left(\frac{r}{Nb}\right) + \ln\frac{\beta\left(\frac{r}{Nb}\right)}{\sinh\beta\left(\frac{r}{Nb}\right)} \tag{A.3}$$

Substituting Eq. (A.3) into Eq. (A.2) and replacing r/Nb with λ_L, Eq. (A.2) can be rewritten as

$$I = 4\pi(Nb)^3 \int_0^1 \exp\left(-NS(\lambda_L)\right)\lambda_L^2\, d\lambda_L \tag{A.4}$$

Under the approximation that $S(\lambda_L) = \frac{3}{2}\lambda_L^2 + \frac{9}{20}\lambda_L^4 + \cdots$ (Merckel et al., 2011), Eq. (A.4) can be expressed as

$$I = 4\pi(Nb)^3 \int_0^1 \exp\left[-N\left(\frac{3}{2}\lambda_L^2 + \frac{9}{20}\lambda_L^4 + \cdots\right)\right]\lambda_L^2\, d\lambda_L \tag{A.5}$$

To derive the fundamental form of the solution, we retain only the leading term of $S(\lambda_L)$, subsequently accounting for higher-order contributions in the refined model. This simplification reduces Eq. (A.5) to the following form

$$I \approx 4\pi(Nb)^3 \int_0^1 \exp\left[-N\left(\frac{3}{2}\lambda_L^2\right)\right]\lambda_L^2\, d\lambda_L \tag{A.6}$$

Since the number of Kuhn segments is typically large, a standard integral form, $\int_0^\infty e^{-\eta x^2} x^2 dx = \frac{\sqrt{\pi}}{4}\eta^{-3/2}$, can be employed, allowing for the approximation of Eq. (A.6) as follows

$$I \sim C_0(b) N^{3/2} \tag{A.7}$$

where the constant C_0 serves as an approximation for the parameter $\left(\frac{2\pi b^2}{3}\right)^{\frac{3}{2}}$. Substituting Eq. (A.7) into Eq. (A.1), the basic approximating function $\Xi(N)$ can be obtained as

$$\Xi(N) \sim \ln C_0(b) + \frac{3}{2}\ln(N) \tag{A.8}$$

A more general expression for $\Xi(N)$ that accounts for higher-order terms of $S(\lambda_L)$ and an integration interval of $(1, \infty)$ can be formulated as $\Xi(N) = A + B\ln(N + C)$. According to the Taylor expansion $\ln(N + C) = \ln(N) + C/N - C^2/2N^2 + \cdots$, the introduction

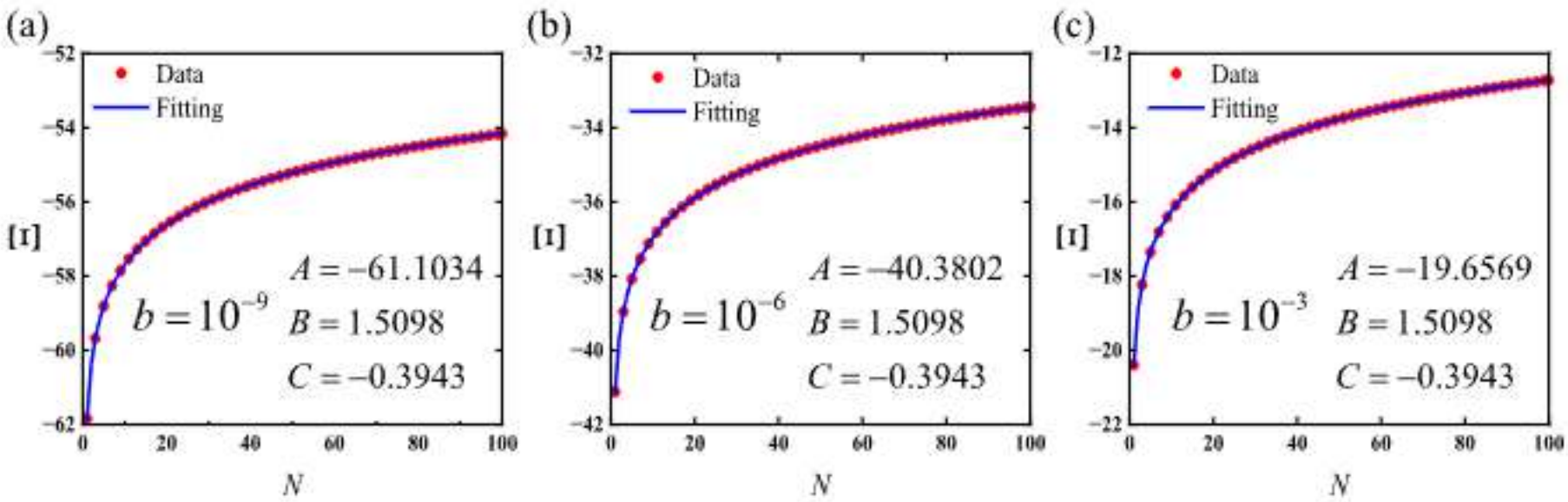

Fig. A.1. Fitting results of the integration function $\Xi(N)$.

of the parameter C serves as a correction to the assumption that N is a large number. This allows the approximation to achieve considerable accuracy even when N is relatively small. In addition, B serves as a correction to the exponent of N. Based on the above analysis, we can understand the meaning of parameter A, B and C

$$\begin{aligned} A &\sim \frac{3}{2}\ln\left(\frac{2\pi b^2}{3}\right) \\ B &\sim \frac{3}{2} \\ C &\sim 0 \end{aligned} \tag{A.9}$$

The parameters A, B, and C are determined via numerical fitting, and the results are shown in Fig. A.1. As expected, the parameter b is found to affect A, but has no influence on B or C. Consequently, $\Xi(N)$ is expressed as

$$\Xi(N) = A(b) + B\ln(N + C), \quad B = 1.5098, \quad C = -0.3943 \tag{A.10}$$

Appendix B. 21 integration points

As detailed in Table B.1, the half-sphere of the microsphere model is discretized using a set of discrete directions, with numerical integration performed via a 21-point scheme (Bažant and Oh, 1986; Miehe et al., 2004).

Table B.1
21 integration points and weights utilized in the constitutive model.

No.	r_1^i	r_2^i	r_3^i	$w^i/2$
1	0.0	0.0	1.0	0.0265214244093
2	0.0	1.0	0.0	0.0265214244093
3	1.0	0.0	0.0	0.0265214244093
4	0.0	0.707106781187	0.707106781187	0.0199301476312
5	0.0	−0.707106781187	0.707106781187	0.0199301476312
6	0.707106781187	0.0	0.707106781187	0.0199301476312
7	−0.707106781187	0.0	0.707106781187	0.0199301476312
8	0.707106781187	0.707106781187	0.0	0.0199301476312
9	−0.707106781187	0.707106781187	0.0	0.0199301476312
10	0.836095596749	0.387907304067	0.387907304067	0.0250712367487
11	−0.836095596749	0.387907304067	0.387907304067	0.0250712367487
12	0.836095596749	−0.387907304067	0.387907304067	0.0250712367487
13	−0.836095596749	−0.387907304067	0.387907304067	0.0250712367487
14	0.387907304067	0.836095596749	0.387907304067	0.0250712367487
15	−0.387907304067	0.836095596749	0.387907304067	0.0250712367487
16	0.387907304067	−0.836095596749	0.387907304067	0.0250712367487
17	−0.387907304067	−0.836095596749	0.387907304067	0.0250712367487
18	0.387907304067	0.387907304067	0.836095596749	0.0250712367487
19	−0.387907304067	0.387907304067	0.836095596749	0.0250712367487
20	0.387907304067	−0.387907304067	0.836095596749	0.0250712367487
21	−0.387907304067	−0.387907304067	0.836095596749	0.0250712367487

References

Arruda, E.M., Boyce, M.C., 1993. A three-dimensional constitutive model for the large stretch behavior of rubber elastic materials. J. Mech. Phys. Solids 41 (2), 389–412.

Assadi, S., Lamont, S.C., Hansoge, N., Liu, Z., Crespo-Cuevas, V., Salmon, F., Vernerey, F.J., 2025. Nonaffine motion and network reorganization in entangled polymer networks. Soft Matter 21 (11), 2096–2113.

Bažant, P., Oh, B.H., 1986. Efficient numerical integration on the surface of a sphere. ZAMM - J. Appl. Math. Mech. Z. F"ur Angew. Math. Mech. 66 (1), 37–49.

Chen, D., Panyukov, S., Sapir, L., Rubinstein, M., 2023. Elasticity of slide-ring gels. ACS Macro Lett. 12 (3), 362–368.

Deng, Z., Yu, R., Guo, B., 2021. Stimuli-responsive conductive hydrogels: design, properties, and applications. Mater. Chem. Front. 5 (5), 2092–2123.

Edwards, S.F., Vilgis, T.A., 1988. The tube model theory of rubber elasticity. Rep. Prog. Phys. 51 (2), 243.

Flory, P.J., Rehner, , J. Jr, 1943. Statistical mechanics of cross-linked polymer networks II. swelling. J. Chem. Phys. 11 (11), 521–526.

Hassan, S., Kim, J., et al., 2022. Polyacrylamide hydrogels. IV. near-perfect elasticity and rate-dependent toughness. J. Mech. Phys. Solids 158, 104675.

Ho, T.-C., Chang, C.-C., Chan, H.-P., Chung, T.-W., Shu, C.-W., Chuang, K.-P., Duh, T.-H., Yang, M.-H., Tyan, Y.-C., 2022. Hydrogels: properties and applications in biomedicine. Molecules 27 (9), 2902.

Hong, W., Liu, Z., Suo, Z., 2009. Inhomogeneous swelling of a gel in equilibrium with a solvent and mechanical load. Int. J. Solids Struct. 46 (17), 3282–3289.

Hong, W., Zhao, X., Zhou, J., Suo, Z., 2008. A theory of coupled diffusion and large deformation in polymeric gels. J. Mech. Phys. Solids 56 (5), 1779–1793.

Hu, L., Chee, P.L., Sugiarto, S., Yu, Y., Shi, C., Yan, R., Yao, Z., Shi, X., Zhi, J., Kai, D., et al., 2023a. Hydrogel-based flexible electronics. Adv. Mater. 35 (14), 2205326.

Hu, Y., Zeng, C., Amar, M.B., Jia, F., Liu, Y., Leng, J., 2023b. Thermo-aqueous coupling behaviors for shape memory hydrogels: a statistical–mechanical model and simulations faced with experiments. Int. J. Solids Struct. 280, 112395.

Hui, C.-Y., Long, R., 2012. A constitutive model for the large deformation of a self-healing gel. Soft Matter 8 (31), 8209–8216.

Ito, K., 2007. Novel cross-linking concept of polymer network: synthesis, structure, and properties of slide-ring gels with freely movable junctions. Polym. J. 39 (6), 489–499.

James, H.M., Guth, E., 1943. Theory of the elastic properties of rubber. J. Chem. Phys. 11 (10), 455–481.

Jedynak, R., 2015. Approximation of the inverse langevin function revisited. Rheol. Acta 54 (1), 29–39.

Jeon, S.-J., Hauser, A.W., Hayward, R.C., 2017. Shape-morphing materials from stimuli-responsive hydrogel hybrids. Acc. Chem. Res. 50 (2), 161–169.

Jiang, L., Liu, C., Mayumi, K., Kato, K., Yokoyama, H., Ito, K., 2018. Highly stretchable and instantly recoverable slide-ring gels consisting of enzymatically synthesized polyrotaxane with low host coverage. Chem. Mater. 30 (15), 5013–5019.

Kim, J., Zhang, G., Shi, M., Suo, Z., 2021. Fracture, fatigue, and friction of polymers in which entanglements greatly outnumber cross-links. Science 374 (6564), 212–216.

Koga, T., Tanaka, F., 2005. Elastic properties of polymer networks with sliding junctions. Eur. Phys. J. E 17 (2), 225–229.

Kuhn, W., Grün, F., 1942. Beziehungen zwischen elastischen konstanten und dehnungsdoppelbrechung hochelastischer stoffe. Kolloid-Z. 101 (3), 248–271.

Lamont, S.C., Weishaar, K., Bruns, C.J., Vernerey, F.J., 2023. Micromechanics and damage in slide-ring networks. Phys. Rev. E 107 (4), 044501.

Li, D., Zhan, W., Zuo, W., Li, L., Zhang, J., Cai, G., Tian, Y., 2022. Elastic, tough and switchable swelling hydrogels with high entanglements and low crosslinks for water remediation. Chem. Eng. J. 450, 138417.

Li, X., Gong, J.P., 2024. Design principles for strong and tough hydrogels. Nat. Rev. Mater. 9 (6), 380–398.

Lifwergren, P., Schoen, V., Naeimipour, S., Khare, L., Wunder, A., Blom, H., Martinez, J.G., Pagella, P., Fridberger, A., Junker, J., et al., 2025. Printing and rerouting of elastic and protease responsive shape memory hydrogel filaments. Adv. Healthcare Mater. 14 (22), 2502262.

Lin, J., Zheng, S.Y., Xiao, R., Yin, J., Wu, Z.L., Zheng, Q., Qian, J., 2020. Constitutive behaviors of tough physical hydrogels with dynamic metal-coordinated bonds. J. Mech. Phys. Solids 139, 103935.

Liu, P., Zhang, Y., Guan, Y., Zhang, Y., 2023. Peptide-crosslinked, highly entangled hydrogels with excellent mechanical properties but ultra-low solid content. Adv. Mater. 35 (13), 2210021.

Liu, X., Yang, Q., Liu, X., Tao, R., Rao, W., 2025. A visco-hyperelastic constitutive model of hydrogel considering the coupling effect between segment motion and interchain slippage. J. Mech. Phys. Solids 196, 105996.

López-Díaz, A., Vázquez, A.S., Vázquez, E., 2024. Hydrogels in soft robotics: past, present, and future. ACS Nano 18 (32), 20817–20826.

Lu, D., Chen, B., 2023. A constitutive theory for large stretch behaviors of slide-ring gels by considering molecular frictions. Soft Matter 19, 1531–1539.

Mayumi, K., Tezuka, M., Bando, A., Ito, K., 2012. Mechanics of slide-ring gels: novel entropic elasticity of a topological network formed by ring and string. Soft Matter 8 (31), 8179–8183.

Merckel, Y., Diani, J., Roux, S., Brieu, M., 2011. A simple framework for full-network hyperelasticity and anisotropic damage. J. Mech. Phys. Solids 59 (1), 75–88.

Miehe, C., Göktepe, S., 2005. A micro–macro approach to rubber-like materials. part II: the micro-sphere model of finite rubber viscoelasticity. J. Mech. Phys. Solids 53 (10), 2231–2258.

Miehe, C., Göktepe, S., Lulei, F., 2004. A micro-macro approach to rubber-like materials–Part I: the non-affine micro-sphere model of rubber elasticity. J. Mech. Phys. Solids 52 (11), 2617–2660.

Obukhov, S.P., Rubinstein, M., Colby, R.H., 1994. Network modulus and superelasticity. Macromolecules 27 (12), 3191–3198.

Okumura, Y., Ito, K., 2001. The polyrotaxane gel: a topological gel by figure-of-eight cross-links. Adv. Mater. 13 (7), 485–487.

Panyukov, S.V., 1990. Scaling theory of high elasticity. Sov. Phys. JETP 71 (2), 372–379.

Panyukov, S.V., 2023. Elasticity of highly entangled polymer networks and gels: review of models and theory of nonaffine deformations. Polym. Sci. C 65 (1), 27–45.

Pensalfini, M., Golde, T., Trepat, X., Arroyo, M., 2023. Nonaffine mechanics of entangled networks inspired by intermediate filaments. Phys. Rev. Lett. 131 (5), 058101.

Shi, M., Kim, J., Nian, G., Suo, Z., 2023. Highly entangled hydrogels with degradable crosslinks. Extreme Mech. Lett. 59, 101953.

Sun, X., Rao, P., He, X., Yang, C., Hong, W., 2023. Chemically identical gels i–under-crosslinked networks. J. Mech. Phys. Solids 175, 105278.

Vernerey, F.J., Lamont, S., 2021. Transient mechanics of slide-ring networks: a continuum model. J. Mech. Phys. Solids 146, 104212.

Wall, F.T., Flory, P.J., 1951. Statistical thermodynamics of rubber elasticity. J. Chem. Phys. 19 (12), 1435–1439.

Wang, J., Tang, F., Chuang, Y., Li, L., 2023a. Low hysteresis hydrogel induced by spatial confinement. Adv. Funct. Mater. 33. https://doi.org/10.1002/adfm.202214935

Wang, M.C., Guth, E., 1952. Statistical theory of networks of non-Gaussian flexible chains. J. Chem. Phys. 20 (7), 1144–1157.

Wang, Q., Gao, Z., Yu, K., 2017. Interfacial self-healing of nanocomposite hydrogels: theory and experiment. J. Mech. Phys. Solids 109, 288–306.

Wang, R., Liu, Q., Wei, J., Zhu, C., Wang, Y., Yu, A., Wang, W., Zou, J., Xie, J., Fu, Z., 2025. Biocomposite silk fibroin hydrogel with stretchability, conductivity and biocompatibility for wireless strain sensor. J. Mater. Sci. Technol. 210, 195–203.

Wang, Z., Chen, J., Wang, Y., Wang, Z., Zhang, Z., Suo, Z., 2023b. Modeling the mechanical behaviors of double-network hydrogels. J. Mech. Phys. Solids 170, 105103. https://doi.org/10.1016/j.jmps.2022.105103

Wu, P.D., Van Der Giessen, E., 1993. On improved network models for rubber elasticity and their applications to orientation hardening in glassy polymers. J. Mech. Phys. Solids 41 (3), 427–456.

Xiang, Y., Zhong, D., Wang, P., Mao, G., Yu, H., Qu, S., 2018. A general constitutive model of soft elastomers. J. Mech. Phys. Solids 117, 110–122.

Xiao, R., Mai, T.-T., Urayama, K., Gong, J.P., Qu, S., 2021. Micromechanical modeling of the multi-axial deformation behavior in double network hydrogels. Int. J. Plast. 137, 102901.

Xing, Z., Shu, D.-W., Lu, H., Fu, Y.-Q., 2022a. Untangling the mechanics of entanglements in slide-ring gels towards both super-deformability and toughness. Soft Matter 18 (6), 1302–1309.

Xing, Z., Shu, D.-W., Lu, H., Fu, Y.-Q., 2022b. Untangling the mechanics of entanglements in slide-ring gels towards both super-deformability and toughness. Soft Matter 18, 1302–1309.

Xu, J., Li, J., Hu, X., Zhong, D., Chen, W., Qu, S., 2024. A constitutive model for hydrogels with tunable mechanical properties by salting-out. J. Mech. Phys. Solids 185, 105571.

Xu, S., Zhou, Z., Liu, Z., Sharma, P., 2023. Concurrent stiffening and softening in hydrogels under dehydration. Sci. Adv. 9 (1), eade3240.
Zhang, Q., Liu, J., Zhang, G., Li, Y., Hu, N., Yang, J., Yang, Y., Qu, S., Kan, Q., Kang, G., 2025. Poroelastic fracture of polyacrylamide hydrogels: enhanced crack tip swelling driven by chain scission. J. Mech. Phys. Solids 194, 105954.
Zheng, D., Lin, S., Ni, J., Zhao, X., 2022. Fracture and fatigue of entangled and unentangled polymer networks. Extreme Mech. Lett. 51, 101608.
Zhong, D., Xiang, Y., Wang, Z., Chen, Z., Liu, J., Wu, Z.L., Xiao, R., Qu, S., Yang, W., 2023. A visco-hyperelastic model for hydrogels with tunable water content. J. Mech. Phys. Solids 173, 105206.
Zhong, D., Xiang, Y., Yin, T., Yu, H., Qu, S., Yang, W., 2019. A physically-based damage model for soft elastomeric materials with anisotropic mullins effect. Int. J. Solids Struct. 176-177, 121–134. https://doi.org/10.1016/j.ijsolstr.2019.05.018
Zhu, P., Zhong, Z., 2020. Modelling the mechanical behaviors of double-network hydrogels. Int. J. Solids Struct. 193, 492–501.
Ziegler, H., Wehrli, C., 1987. The Derivation of Constitutive Relations from the Free Energy and the Dissipation Function. Elsevier. Vol. 25 of *Advances in Applied Mechanics*, pp. 183–238.